The final version was published in the proceedings of the conference as paper No. 2019-2502. https://doi.org/10.2514/6.2019-2502

Investigation of Sound Generation and Transmission Effects Through the ACAT1 Fan Stage using Compressed Sensing-based Mode Analysis

Maximilian Behn* and Ulf Tapken †
German Aerospace Center (DLR),
Institute of Propulsion Technology,
Engine Acoustics Department,
Berlin, Germany

In an extensive measurement campaign at the UFFA test rig of AneCom AeroTest in Wildau, Germany, the sound field generated from the ACAT1 fan stage was measured by several dynamic pressure sensor arrays of different geometrical arrangements at the inlet, interstage and bypass section. The sparse ring arrays with irregular and optimised geometries are utilised in combination with the Compressed Sensing-based mode analysis in order to investigate the tonal and broadband sound generation and transmission with high resolution. From the azimuthal mode spectra, the relation between the cut-on mode range at the sources and the dominant modes at the measurement sections is observed and used to determine the contribution of different sound generation mechanisms. With the help of interstage mode analyses strong rotor-coherent contributions due to rotor wake irregularities are identified and the rotor-shielding effect is assessed. The dependencies of the broadband mode spectra with respect to the operation points and working lines are shown and the contribution of stator and rotor bound sources is investigated. Results indicate that mode scattering at the stator vane row has a significant influence on the downstream radiated sound field. Evidence is further found for the occurrence of the acoustic tunnel effect, where cut-off modes excited at the stator leading edge become cut-on during the propagation through the inter-vane channels. This effect triggers mode scattering towards rotor counter-rotating modes and increases the sound radiation from fan stages.

I. Nomenclature

ACAT	=	AneCom AeroTest
AMA	=	Azimuthal mode analysis
AP	=	Approach condition
BPF	=	Blade passing frequency
CB	=	Cutback condition
CyS1	=	First-order cyclostationarity (tonal)
CyS2	=	Second-order cyclostationarity (broadband)
EO	=	Engine order
LG	=	Long gap configuration
LN	=	Low noise working line
SG	=	Short gap configuration
SL	=	Sideline condition
SLS	=	Sea level static working line

A_m	=	Azimuthal mode amplitude
$\lvert A_m^\mu \rvert^2$	=	Coherent output power spectrum, Eq. 7
C_m^μ	=	Mode coherence, Eq. 6
$\frac{kR}{V}$	=	Cascade-related Helmholtz number
m	=	Azimuthal mode order
p	=	Sound pressure amplitude
$\mathbf{S}_{pp}$	=	Cross-spectral matrix of sound pressure
$\mathbf{S}_{aa}$	=	Cross-spectral matrix of mode amplitudes
V	=	Number of stator vanes
$\mathbf{W}$	=	Mode transfer matrix, Eq. 2

*Junior Scientist, Engine Acoustics Department, Müller-Breslau-Str. 8, 10623 Berlin, Germany, email: maximilian.behn@dlr.de
†Research Scientist, Engine Acoustics Department, Müller-Breslau-Str. 8, 10623 Berlin, Germany

II. Introduction

In the beginning of 2018 manifold aerodynamic and acoustic instrumentation was used to investigate the flow field and the sound field generated by the ACAT1 fan stage during an extensive measurement campaign at the UFFA test rig of AneCom AeroTest in Wildau, Germany. The experimental database comprises two rotor-stator gap configurations at two different working lines and various rotor speeds. Several dynamic pressure sensor arrays at the inlet, interstage and bypass section measured the unsteady pressure fields simultaneously. In this study the focus lies on the evaluation of ring arrays by use of the azimuthal mode analysis. It is shown that detailed insight into sound generation and transmission effects can be obtained, when use is made of advanced signal processing techniques for separating tonal and broadband components and of the Compressed Sensing-based mode analysis in order to achieve a larger dynamic range at high frequencies with a high number of cut-on modes.

The mode analysis of the in-duct sound field radiated from turbomachinery by use of dynamic pressure sensor arrays is an established technique that enables the investigation of the sound generating mechanisms. The mode spectra of the tonal sound field components at the blade passing frequency (BPF) and its harmonics typically are characterised by few dominant azimuthal mode orders that are associated with the interaction of the rotor wakes and the stator vane row [1]. In contrast, broadband sound fields are composed of the full range of cut-on modes. Various models have been proposed imposing assumptions regarding the energy distribution among the different radial modes and their correlations [2]. Experimental mode decomposition techniques have been presented for the analysis of the tonal [3, 4] and broadband sound field components [5, 6]. Comprehensive mode analyses have been presented by Heidelberg [7] and Premo & Joppa [8] for the NASA fan noise source diagnostic test (SDT), where the mode structure of the tonal components was investigated using rotating rake arrays. Azimuthal mode analysis was applied to investigate the modal structure at the inlet, interstage and aft duct for various configurations and rotor speeds. For that investigation three evenly spaced circumferential arrays were installed with a total of 180 sensors, each array covering only half of the circumference. This array design shifted the aliasing limit to a higher mode order of $m_{Alias} = 120$, but it came with the drawback that only even mode orders were possible to be analysed due to an unfavourable array sidelobe pattern.

Modern signal processing techniques such as deconvolution techniques [9], quantitative beamforming [10] and Compressed Sensing [11–14] remove the array sidelobe pattern and yield mode spectra with higher dynamic range and resolution. This is crucial when ring arrays with irregular sensor spacing are applied in order to analyse a larger mode range. The use of irregular, subsampling sensor arrays in combination with the Compressed Sensing-based mode analysis, which is applied in this study, is also more robust towards sensor failure than typically applied methods such as the discrete Fourier transform and the least-squares fit [15]. An advantage of the Compressed Sensing-based azimuthal mode analysis is that it can determine mode amplitudes as well as mode coherences.

In the presented study the sound generation and transmission effects through the ACAT1 fan stage are investigated on the basis of mode spectra at the inlet, interstage and bypass sections. Through the use of optimised arrays and advanced signal processing techniques improved accuracy and resolution is achieved for the determined azimuthal mode spectra, which allows deeper insight into the sound generation and transmission of turbomachinery stages. The dependencies of the tonal and broadband sound generation on the aerodynamic operating point and the working line are discussed in detail and sound transmission effects are identified, which have a significant impact on the sound radiated up- and downstream of the fan stage.

In section III the UFFA test rig equipped with the ACAT1 fan stage and the investigated operating conditions are presented. The design and properties of the applied ring arrays along with the newly optimised ring array at the interstage are described.

A time-domain procedure to separate tonal and broadband sound field components is presented in section IV, which retains the phase relations for both signal components and improves the mode analysis outcome. Brief descriptions of the Compressed Sensing-methods for the azimuthal mode analysis of tonal and broadband components are given. Quantities such as mode coherences and the coherent output spectrum that are derived from the cross-spectral matrix of mode amplitudes are introduced and their use is described.

In section V first the generation of the tonal sound field is discussed and subsequently the broadband sound generation mechanism on the basis of the determined azimuthal mode spectra. It is shown that contributions of the different sound generation mechanisms can be determined by inspection of the cut-on mode ranges at the rotor and stator. Furthermore, the impact of dissimilar rotor wakes is identified through the occurrence of high mode amplitudes at discrete mode orders, which are related to rotating pressure distributions. Particularly, the interstage mode analyses enable an acoustic identification of rotor wake irregularities without affecting the flow field upstream of the stator or generating additional noise sources. The azimuthal mode spectra enable also the assessment of the rotor-shielding effect.

In section VI mode scattering at the stator vane row is identified through the evaluation of inter-mode coherences.

The detected mode scattering exhibits a characteristic relationship between frequency and mode order. A dependency on the flow conditions at the stator is found by comparison of the two working lines. Also evidence of the acoustic tunnel effect [16] is presented for the first time, where cut-off modes that are excited at the stator leading edge become cut-on in the inter-vane channels and contribute significantly to the downstream radiated sound field.

III. Experimental setup

A. UFFA test rig

A comprehensive database of aerodynamic and acoustic measurements of the ACAT1 fan stage was generated at the UFFA test rig of AneCom Aerotest, Wildau, Germany. The fan stage consists of a rotor with 20 blades and a stator with 44 vanes. Two configurations were built with different axial rotor-stator spacings (short gap (SG) and long gap (LG), see Fig. 1). During the experiments two working lines with differing rotor loading, sea level static (SLS) and low noise (LN), were tested at various rotor speeds between 50 % and 100 % nominal rotor speed. The results in the presented study are shown for operating conditions similar to the three acoustic certification points *approach* (AP), *cutback* (CB) and *sideline* (SL) conditions. The operating conditions are given in Fig. 2 in terms of the total corrected mass flow and the pressure ratio between the bypass and the inlet. A detailed description of the operation conditions and results of aerodynamic measurements are presented by Guérin et al. [17]. During the noise tests, the stator vanes were not equipped with pressure rakes in order to avoid additional noise sources. Hence, the fan pressure ratio was not measured directly and instead pressure rakes were used downstream of the bypass measurement section. For the low noise working line the pressure ratio is reduced, while the mass flow is increased. This results in a lower fan loading. The different operating conditions match well for the comparison of the short and long gap configurations. The maximum relative deviation of the pressure ratio and the total corrected mass flow is approximately two per cent.

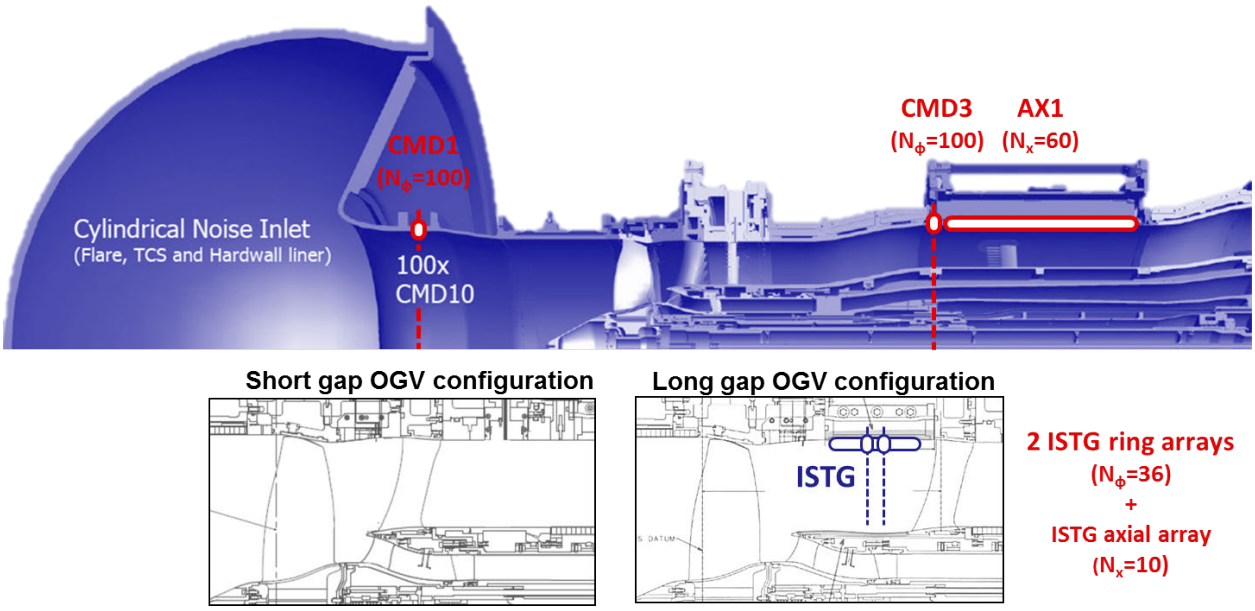

Fig. 1 For the acoustic measurements the UFFA test rig was equipped with ring arrays at the inlet (CMD1), interstage (ISTG) and bypass section (CMD3). The ACAT1 fan stage was tested in two configurations with different axial rotor-stator spacing. (Source: AneCom AeroTest)

B. Ring arrays at inlet and bypass

Single ring arrays of dynamic pressure sensors were installed at the inlet and bypass section (100 sensors each). The sensor positions are result of an optimisation, which was performed and described by Rademaker et al. [18]. The inlet and bypass ring arrays enable the azimuthal mode analysis for mode range between $m = \{-79, \ldots, 79\}$. According to Behn et al. [12] the application of Compressed Sensing-based AMA to the inlet and bypass ring arrays enables the

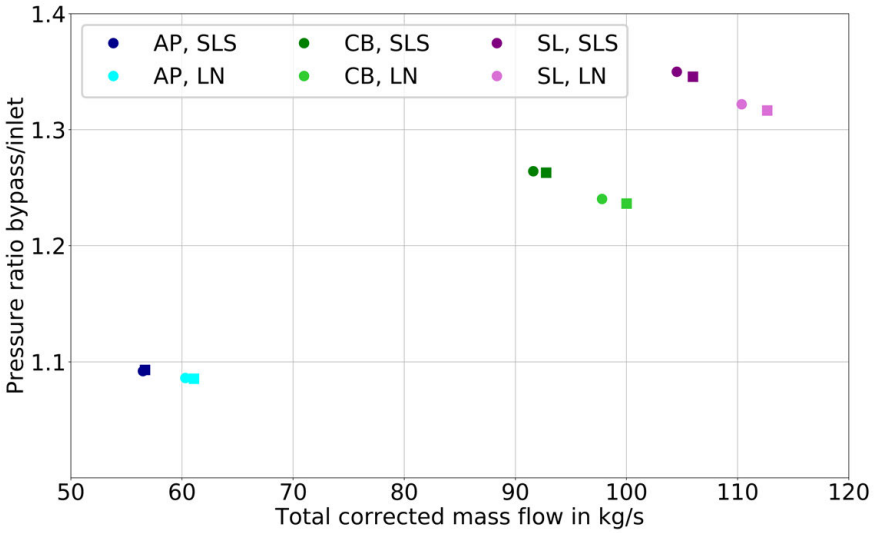

Fig. 2 Operating conditions for *approach* (AP), *cutback* (CB) and *sideline* (SL). Circles are used for the short gap configuration (SG) and squares for the long gap configuration (LG).

determination of up to 13 dominant modes and a robust estimation of the remaining mode amplitudes due to the array sidelobe level of approximately 22.6 dB. During the tests up to 4 sensors per ring array failed, which reduces the number of determined, dominant modes to 9 and results in a decreased array sidelobe level of 19.7 dB.

C. Ring array at interstage

At the interstage section two newly designed ring arrays (36 sensors each) with same azimuthal positions were installed with an axial spacing of 13.5 mm, which were only available for the long gap configuration due to space constraints. The optimisation of the array design was performed by the authors using the procedure described by Behn et al. [12] under the constraints of a minimum sensor spacing of 2 degrees and assigned keep-out zones around the top and bottom dead center. The outcome is depicted in Fig. 3. The interstage array design allows the reconstruction of three dominant modes in the same mode range as for the inlet and bypass arrays. In order to achieve a stable reconstruction of the dominant modes the deconvolution step of the applied EOMP-algorithm must be disabled, i.e. the remaining mode amplitudes cannot be determined after the three strongest modes are identified (see section IV). This is because there is an insufficient level difference between the dominant modes and the remaining modes due to the increased flow noise at the interstage section with respect to the achieved array sidelobe level of approximately 11 dB. An advantage of irregular, sparse ring array designs is the improved robustness towards the impact of sensor failures in comparison to ring arrays with uniform sensor spacing [15]. During the measurements one of 36 sensors in the considered interstage ring array failed, which does not affect the number of determinable, dominant modes and results in an effective array sidelobe level of approximately 10 dB for the following analyses. The measurement duration was 30 s with the before-mentioned ring arrays at a sampling rate of 100 kHz during the tests.

IV. Description of the analysis procedure

The investigation comprised the analysis of both the tonal and the broadband sound fields. Therefore, the measured time series are first processed in order to separate both signal components and are subsequently used as input to the Compressed Sensing-based azimuthal mode analysis. In the following the required methods are discussed briefly.

A. Separation of tonal and broadband components through cyclostationary analysis

The measured time series are resampled with regard to the rotor shaft trigger. After resampling, the pressure signal $p(t)$ is separated in blocks of each 16 rotor revolutions. The ensemble average of these blocks yields the rotor-locked signal $s(t)$, which can be interpreted as the tonal signal components. Under the assumption of cyclostationarity [20], the

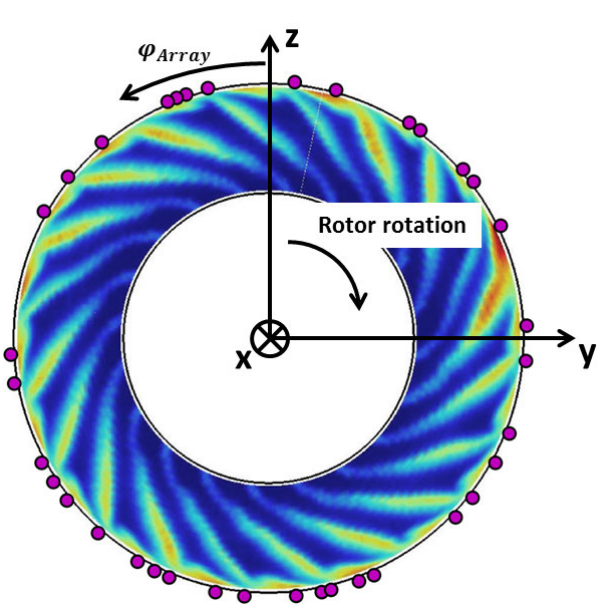

Fig. 3 Positions of the newly designed interstage ring arrays with 36 sensors. A mode range between $m = \{-79, \ldots, 79\}$ is applied for the analysis. The coordinate system is given along with the direction of rotor rotation. (Background illustration reproduced from [19] with permission.)

residual signal $r(t) = p(t) - s(t)$ contains the broadband signal components, whose phase fluctuates randomly with the rotor revolutions. The broadband signal is second-order cyclostationary (CyS2) and the tonal signal comprises first-order cyclostationarity (CyS1) [21].

For illustration the power spectral density of both signal components CyS1 and CyS2 are compared in Fig. 4 against the result of a quasi-stationary analysis using the Welch-method [22] and where resampling is omitted. The comparison shows that tonal components are dominant at the BPF and its higher harmonics as well as at integer engine orders below the first BPF. The broadband components match almost exactly the quasi-stationary result at non-integer engine orders. At each BPF component the broadband level increases considerably compared to the neighbouring frequencies. Peaks of the broadband components besides the BPF components originate from fluctuating flow separation at the rotor blades and non-rotor-locked sources. In contrast to the interstage section, the tonal component at BPF is approximately 15 dB lower at the bypass array due to the cut-off design of the ACAT1 fan stage. The broadband components show stronger fluctuations at the interstage array above BPF, which result from cut-off modes that are present in the near-field of the sources, i.e. rotor and stator.

B. Compressed Sensing-based azimuthal mode analysis

The sound field in annular flow ducts can be decomposed into its azimuthal mode constituents by use of the spatial Fourier transform [12]:

$$p(x, \varphi) = \sum_{m=-\infty}^{+\infty} A_m(x) \cdot e^{im\varphi}. \tag{1}$$

The radial dependency is neglected under the assumption that the decomposition is based on measurements with wall flush-mounted sensors.

1. Analysis of tonal sound fields

In the case of fully correlated sound field components the relation between the complex sound pressure values $\boldsymbol{p}$ measured at N_{mic} sensor positions and the underlying azimuthal mode spectrum $\boldsymbol{a}$, where N_{modes} propagating modes

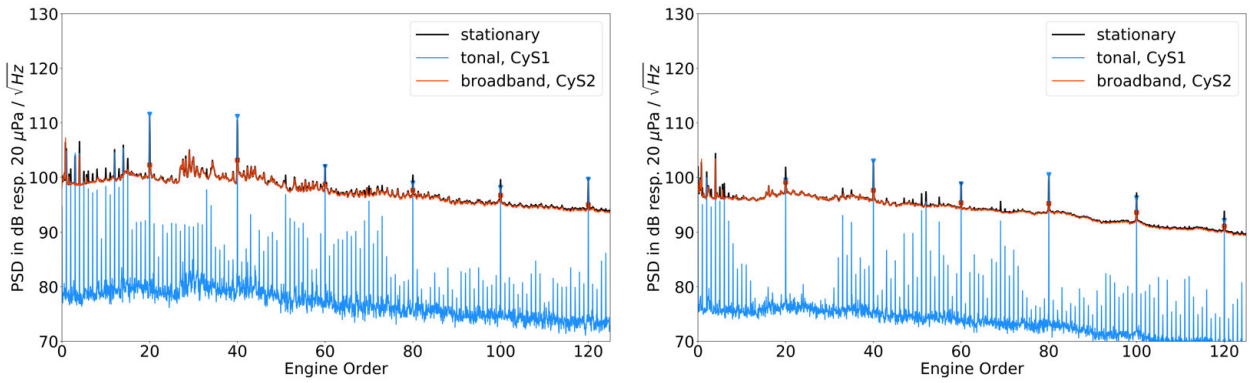

(a) Interstage (b) Bypass

Fig. 4 Comparison of the average auto power spectral density for the ring arrays at the interstage and the bypass section. The quasi-stationary result (black) is compared to the separated tonal (blue) and broadband (red) spectra after application of the cyclostationary analysis. The results are shown for the long gap configuration, SLS working line at *approach*.

are considered, is formulated as a system of linear equations:

$$\boldsymbol{p} = \boldsymbol{W}\boldsymbol{a} \tag{2}$$

where $\boldsymbol{W}$ is a matrix of size N_{mic}xN_{modes} containing the mode transfer functions $e^{im\varphi_k}$ evaluated for the mth mode order at the kth sensor position. This formulation is applied for the analysis of tonal components. In this study the chosen mode range for the different arrays (inlet, interstage and bypass) is $m = \{-79, \ldots, +79\}$. The azimuthal mode analysis of the tonal components is performed by solving the system of linear equations in Eq. 2.

In the context of the azimuthal mode analysis, Compressed Sensing techniques are used as an approach to solve underdetermined systems of linear equations under the assumption that the solution vector is sparse, i.e. the azimuthal mode spectrum consists only of a few dominant modes. As discussed in ref. [12], the correct solution of Eq. 2 is found by minimisation of the l_1-norm of the mode amplitude vector. In terms of AMA with an assumed noise energy ϵ this can be formulated mathematically as follows:

$$\boldsymbol{a} = \underset{\boldsymbol{a}\in\mathbb{C}^{N_{modes}}}{\operatorname{argmin}} \|\boldsymbol{a}\|_1 \quad \text{subject to } \|\boldsymbol{p} - \boldsymbol{W}\boldsymbol{a}\|_2 < \epsilon. \tag{3}$$

The minimisation problem is solved by use of the Orthogonal Matching Pursuit-algorithm with an additional deconvolution step (EOMP-algorithm, see [12]).

2. Analysis of broadband sound fields

The broadband mode constituents are described statistically in terms of mean values and spatial cross-spectra. The spatial cross-spectrum is determined for each combination of the ring array sensor positions φ and φ' by the following equation:

$$S_{pp} = \lim_{T\to\infty} E\left\{\frac{1}{T} p(\omega, x, r, \varphi) p^*(\omega, x, r, \varphi')\right\}. \tag{4}$$

The expectation value $E\{\ldots\}$ is approximated by time-averaging over a suitably long period. From Eq. 1 and 4 the relation between the mode amplitudes and the resulting sound pressure signal at the microphone array is described in matrix notation as

$$\mathbf{S}_{pp} = \mathbf{W}\mathbf{S}_{aa}\mathbf{W}^H, \tag{5}$$

where $\mathbf{S}_{pp}$ is the cross-spectral matrix of the pressure signals, $\mathbf{S}_{aa}$ is the cross-spectral matrix of the mode amplitudes and $\mathbf{W}$ the mode transfer matrix as explained above. The broadband mode amplitudes are determined by solving Eq. 5 for the cross-spectral matrix $\mathbf{S}_{aa}$. From the determined cross-spectra of the mode amplitudes the mode coherence

between two modes m and μ is calculated as

$$C_m^\mu = \frac{\left|\langle A_m A_\mu^* \rangle\right|^2}{\langle |A_m|^2 \rangle \langle \left|A_\mu\right|^2 \rangle}. \tag{6}$$

Mode scattering is investigated by use of the coherent output power spectrum between two modes m and μ, where μ is the input mode order and m is the output mode order, i.e. the mode order that energy is scattered into, which is defined as [23]:

$$\left|A_m^\mu\right|^2 = C_m^\mu \left|A_m\right|^2. \tag{7}$$

The Compressed Sensing-approach for the analysis of broadband sound fields utilizes a decomposition of the sound pressure cross-spectral matrix into its coherent constituents by use of the eigenvalue decomposition (cf. [13] and [24] for use of L1-norm regularisation)

$$\mathbf{S}_{pp} = \mathbf{U}\Lambda\mathbf{U}^\dagger, \tag{8}$$

where $\mathbf{U}$ is a unitary matrix consisting of orthonormal eigenvectors $\mathbf{u}_i$ and Λ is a diagonal matrix with the corresponding eigenvalues λ_i with $i = 0, \ldots, N_{mic} - 1$. This follows from the fact that the cross-spectral matrix is positive semidefinite and Hermitian. The individual eigenvectors are weighted with their eigenvalue

$$\mathbf{v}_i = \sqrt{\lambda_i}\mathbf{u}_i \tag{9}$$

and used as input to the Compressed Sensing-based azimuthal mode analysis in Eq. 3 yielding the formulation of the Compressed Sensing method for the analysis of broadband sound fields:

$$\underset{\mathbf{a}_i \in \mathbb{C}^{N_{modes}}}{\operatorname{argmin}} \|\mathbf{a}_i\|_1 \;\text{ subject to } \|\mathbf{v}_i - \mathbf{W}\mathbf{a}_i\|_2 < \epsilon. \tag{10}$$

As for the tonal components in Eq. 3, applying the EOMP-algorithm to Eq. 10 yields the mode spectra $\mathbf{a}_i$ corresponding to the eigenvalues λ_i. As a result, the cross-spectral matrix of the mode amplitudes is calculated by superposing the contributions of the individual coherent constituents:

$$\mathbf{S}_{aa} = \sum_{i=0}^{N_{mic}-1} \mathbf{a}_i \mathbf{a}_i^H. \tag{11}$$

V. Sound generation of the ACAT1 fan stage

In the first part of the study the sound generation of the investigated ACAT1 fan stage is analysed. By comparison of the resulting mode amplitudes at the inlet, interstage and bypass section the influence of the axial gap variation, working line and aerodynamic operating point is discussed. Results are shown for both, the tonal and the broadband sound generation.

A. Tonal sound field

The AMA results shown in Fig. 5 illustrate the tonal mode spectra at inlet and bypass. At *approach* the first BPF is cut-off, but at the higher order harmonics of the BPF the rotor-stator interaction modes are dominant. Besides the BPF high levels occur along a line of modes following the relation $m = -EO + V = -EO + 44$. Mode constituents, whose mode order increases steadily with engine order, originate from rotating pressure patterns [25, 26]. In the special case of modes with the relation $m = -EO$ the rotating pressure pattern is stationary. The shift of mode orders by the number of vanes indicates scattering of the rotating pressure pattern at the stator row. This effect is a broader interpretation of the rotor-stator interaction mechanism described by Tyler & Sofrin [1]. It should be pointed out that modes with negative mode order rotate in the direction of the rotor revolution as indicated through the counting direction for the angular position of the arrays in Fig. 3. The scattered modes are generated due to dissimilar rotor wakes, which were observed in aerodynamic measurements [19]. The red and white lines indicate the cut-on region* at the stator and bypass section, respectively, for the left-hand figure. The lines on the right-hand figure indicate the cut-on region regarding the rotor

*The mode cut-on range is calculated using an analytical radial mode model assuming a constant flow profile (plug flow) on the basis of the mass flow averaged Mach number and static temperature [27].

Table 1 Azimuthal mode orders of rotor-alone and rotor-stator interaction tones and their cut-on condition. (*very close to cut-on limit)

BPF	m	Inlet	Interstage	Bypass
1	-20	cut-off: AP, CB, SL	cut-off: AP, CB, SL	cut-off: AP, CB; cut-on: SL*
1	24	cut-off: AP, CB, SL	cut-off: AP; cut-on CB, SL	cut-off: AP, CB, SL
2	-40	cut-off: AP, CB; cut-on: SL*	cut-off: AP, CB, SL	cut-off: AP, CB; cut-on: SL
2	4	cut-on: AP, CB, SL	cut-on: AP, CB, SL	cut-on: AP, CB, SL
3	-60	cut-off: AP, CB; cut-on: SL	cut-off: AP, CB, SL	cut-off: AP, CB; cut-on: SL
3	-16	cut-on: AP, CB, SL	cut-on: AP, CB, SL	cut-on: AP, CB, SL
3	28	cut-on: AP, CB, SL	cut-on: AP, CB, SL	cut-on: AP, CB, SL

front face and the inlet measurement section. The cut-on regions at the respective sections differ, because the duct radii at hub and tip vary leading to flow acceleration and deceleration between the sections (compare Fig. 1). Two aspects can be observed from the cut-on regions. Firstly, at the bypass section there are rotor-coherent modes at low engine orders outside the cut-on region. These modes are remains of the rotor wakes, which are convected downstream up to the bypass measurement section. Secondly, the resulting mode spectra at the measurement sections depend on the cut-on mode ranges at the source (compare red lines), i.e. even though higher order modes are cut-on at the array positions, these modes do not transport any sound power since they are not generated at the fan stage and no energy is scattered into these modes. Further results are given in the appendices A.A and A.B, which show this dependency of mode range at the measurement section holds for all investigated test points.

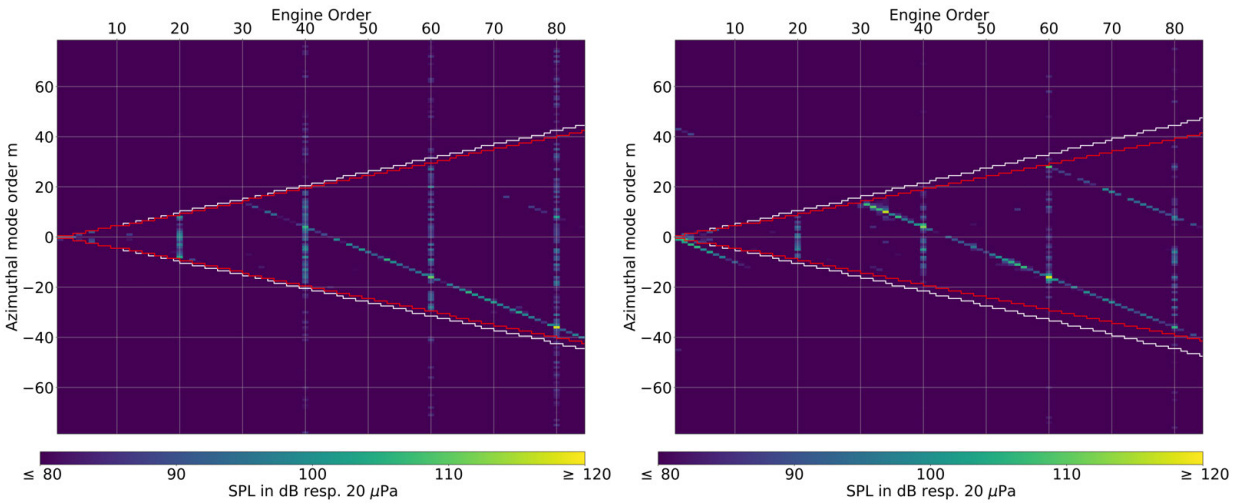

(a) Inlet (b) Bypass

Fig. 5 Comparison of the tonal (CyS1) azimuthal mode spectra for the ring arrays at inlet and bypass. The results are shown for the short gap configuration, SLS working line at *approach*. The red lines indicate the mode cut-on range at the stator trailing edge on the left-hand side and at the rotor front face on the right-hand side. The white lines show the cut-on range at the respective array positions at the inlet and bypass.

1. Overview of the short gap configuration

An overview on the tonal sound generation of the ACAT1 fan stage is given for the short gap configuration regarding the rotor-alone and rotor-stator interaction modes (see Table 1) in Fig. 6. Due to the cut-off design of the fan stage the sound pressure levels at BPF are relatively low, except for the rotor-alone mode in the inlet at *sideline* and LN working

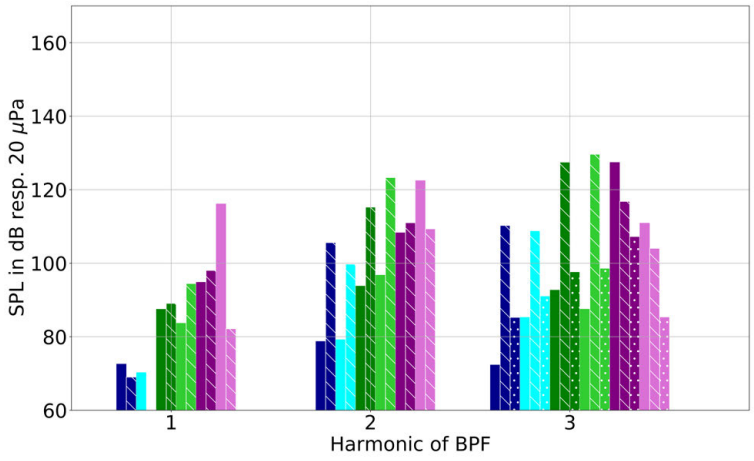

(a) Inlet

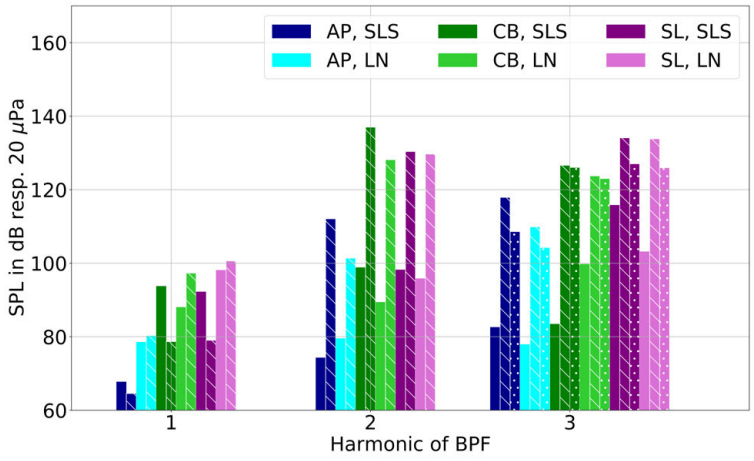

(b) Bypass

Fig. 6 Comparison of the tonal (CyS1) azimuthal mode spectra for the ring arrays at inlet and bypass. The results are shown for the short gap configuration. Full bars indicate the rotor-alone mode, hatched bars are the rotor-stator interaction modes.

line, where the low order buzz-saw components are cut-on also at the array section, because of the increased mass flow at this operating condition (see appendix A.A and A.B). The mode spectra at the second harmonic of the blade passing frequency are dominated by rotor-stator interaction mode for all operating points in the bypass. The results for the LN working line yield reduced levels at the bypass section, but the levels are increased for *cutback* and *sideline* at the inlet. Comparing the results from inlet and bypass the effect of rotor-shielding is evident. Interaction modes, whose direction of rotation is in opposite direction to the rotor rotation, are reflected by the rotor and show lower sound pressure levels in the inlet by 10 to 20 dB compared to the bypass. However, the effect of rotor-shielding can only be quantified approximately from these results, because of unknown aspects such as the energy distribution between the cut-on radial mode orders and the strength of reflections from the inlet. At the third BPF harmonic the interaction modes dominate the sound field for the subsonic operating points *approach* and *cutback*, whereas the rotor-alone mode yields the highest levels in the inlet at *sideline*. The influence of rotor-shielding is clearly visible for the second order interaction mode $m = 28$ (dotted bars), particularly in contrast to the first order interaction mode $m = -16$ (lined bars). At *sideline* also the rotor-stator interaction mode $m = -16$ is strongly reduced at the inlet due to increased reflections caused by the shocks developing at the blade tip region. The presence of shocks at *sideline* provides further the explanation for the dominance of the rotor-alone mode in the inlet. The corresponding results for the long gap configuration are provided in appendix A.C. The results show similar trends as for the short gap configuration. A further assessment of the impact of the larger axial rotor-stator gap is difficult due to possibly strong interference patterns of the tonal components and resulting spacial fluctuations of the azimuthal mode amplitudes.

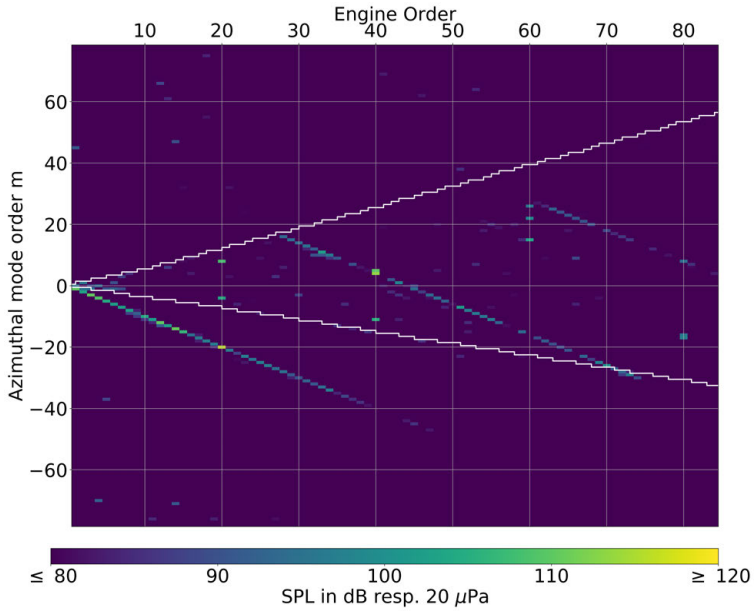

Fig. 7 Tonal (CyS1) azimuthal mode spectra for the ring array at the interstage section. The results are shown for the long gap configuration, SLS working line at *approach*. The white lines indicate the mode cut-on range in the interstage.

2. Detailed analysis of the interstage mode spectrum

In the interstage between rotor and stator the azimuthal mode spectrum can be divided into three different domains (see Fig. 7). Below the blade passing frequency the rotating stationary pressure field downstream of the rotor induces high amplitudes at mode orders $m = -EO$, which is characteristic for the Doppler shift of rotating sources [25, 26]. As shown by the approximate cut-on range[†] the mode orders $m = -EO + 44$, which are scattered at the stator are cut-off and do not contribute noticeably to the detected interstage mode spectrum up to the BPF. Between the first and the second harmonic of the BPF a transition region is apparent, where the amplitudes of the rotating flow field diminish

[†]The mode cut-on range is calculated using an analytical radial mode model assuming a constant flow profile (plug flow) and solid body rotation like swirl on the basis of the mass flow averaged Mach number, radially constant angular velocity and static temperature [27].

and the scattered modes at the stator lie within the cut-on mode range. As expected, particularly the interaction mode at the second BPF harmonic is dominant. In the third domain above engine order 40, only scattered, acoustic cut-on modes are detected. The interstage mode amplitudes shown in Fig. 19 confirm that for low rotor speed the rotor alone mode is dominant at BPF, but for higher rotor speed the cut-on range is shifted due to the swirl so that the first order interaction mode is cut-on, which then reaches high amplitudes in the near-field of the stator. At the second and third BPF harmonic the interaction modes dominate the tonal sound field, but they have lower amplitudes compared to the BPF. From the mismatch of the approximate cut-on mode range and the mode spectrum around engine order 70 it is seen that the assumed swirl component is slightly overestimated, which reduces the predicted number of cut-on rotor co-rotating modes.

The mode distribution of the rotating stationary flow field, which is determined by the interstage mode analysis for the modes with $m = -EO$, can be verified by a decomposition of the stationary, rotor-locked flow field into its azimuthal mode constituents. For this purpose the rotor-synchronously averaged velocity measured by the hotwire probes at position HW2, upstream of the stator (compare [19]), is analysed according to Eq. 1 for the axial flow velocity component and depicted in Fig. 8 over the radial position. The results show significant amplitudes for multiples of the rotor blade count and additional mode orders towards the tip. Particularly, below the BPF the mode orders with the highest velocities correspond well to the mode orders with high pressure amplitudes in Fig. 7. Also at higher rotor speeds, elevated tonal components at non-BPF engine orders are observed for the ACAT1 fan stage that result from rotor wake irregularities (see A.F and A.G), which are identified by hotwire measurements [19] and interstage mode analyses.

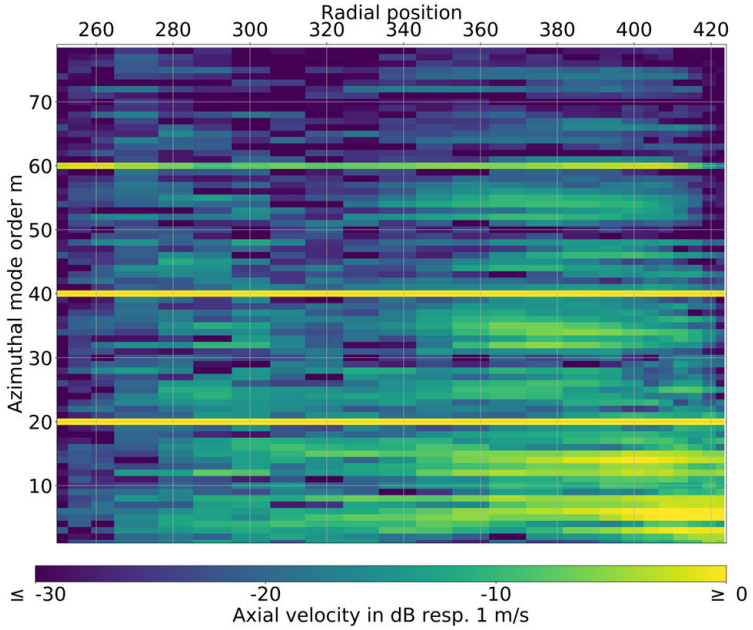

Fig. 8 Decomposition of the stationary, rotor-locked axial flow velocity into azimuthal modes according to Eq. 1. The results are shown for the long gap configuration at position HW2 (compare Fig. [19]), SLS working line at *approach*.

B. Broadband sound field

1. Overview of the sound generation at approach *conditions*

Figure 9 presents the averaged spectra at the bypass for all *approach* test points. The results show a significant noise reduction between the SLS and LN working line. For both configurations measured levels decrease in the frequency range from 1 kHz to about 6 kHz by 1-3 dB. At the LN working line the spectra are smooth with relatively strong peaks at the BPF and its harmonics. At the SLS working line strongly fluctuating spectra occur, which are assumed to be caused by flow separation. The peaks at the BPF and its harmonics are less prominent, particularly at the third and fourth BPF harmonic. Comparing the short gap and long gap configuration, it is found that for the short gap configuration

lower levels are measured below 2-3 kHz, possibly due to the slightly smaller mass flow and hence reduced turbulent pressure fluctuations at the sensor membranes (compare Fig. 2). Furthermore, the spectra generated by the short gap configuration are shifted towards higher frequencies compared to the long gap configuration, which indicates that regarding the sound generation the relevance of flow turbulence with smaller length scales is increased compared to the long gap configuration.

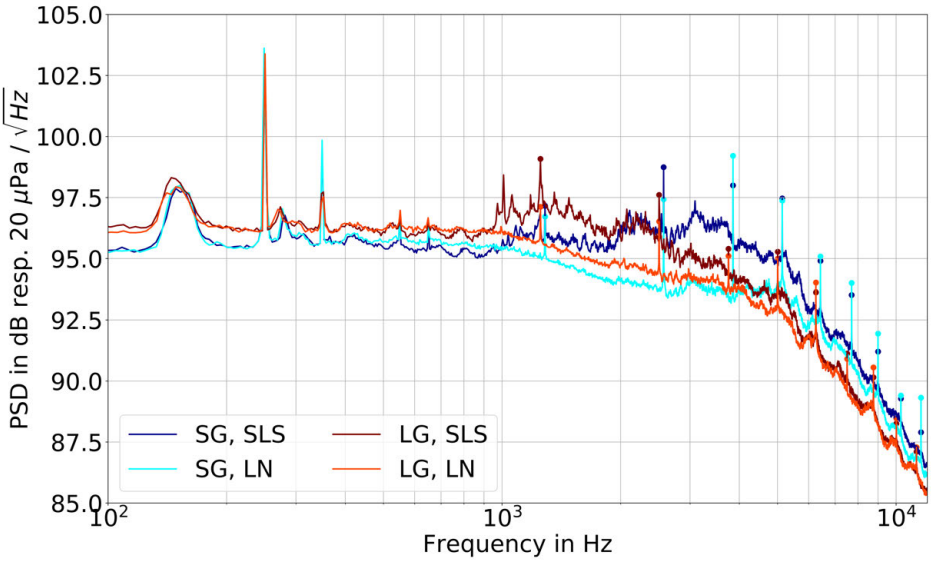

Fig. 9 Comparison of the broadband (CyS2) average auto power spectral density at the bypass. The results are shown for both working lines and configurations at *approach*.

2. Overview for the long gap configuration

At high rotor speeds, differences in the measured spectra for the SLS and LN working line occur predominantly below 2 and 3 kHz as depicted in Fig. 10 for the long gap configuration. This increase over a wide frequency range is attributed to increased turbulent pressure fluctuations at the duct wall due to the higher flow velocity for the LN working line. Towards high frequencies no significant noise reduction is determined for the LN working line in comparison to the SLS working line. Nevertheless, measured spectra at LN working line appear smoother at each measurement section (bypass, inlet and interstage). For *approach* conditions the shift from SLS to LN working line results in a substantial broadband noise reduction at the interstage and inlet section. The working line and operation point comparison of the broadband sound generation for the short gap configuration shows similar trends and is omitted here for the sake of brevity. A more detailed analysis of the relevant noise sources can be made on the basis of the azimuthal mode spectra.

3. Detailed analysis of the broadband sound generation at low rotor speed

In Figure 11 the effect of the different working lines is shown with respect to the generated azimuthal mode spectra for *approach* conditions. In accordance with the averaged auto spectra discussed above, mode amplitudes are higher for the SLS working line. At the bypass section the broadband mode spectra are asymmetric with respect to mode order 0. Regions of high mode amplitudes occur between the orders $m = +8$ to $m = +24$ and $m = -8$ to $m = -24$, where the rotor counter-rotating modes with positive mode order yield higher amplitudes. The asymmetry of the radiated broadband mode spectrum indicates that the sound sources are located near the stator leading edge, where the orientation of the dipole sources is perpendicular to the vane leading edge angle [28]. At the inlet, a clear preference for rotor co-rotating modes of negative order is observed, which is also found in the interstage mode spectra shown in the appendices A.H and A.I as well as in the mode spectrum shown by Kissner et al. [29] from numerical computations of the ACAT1 fan, which signifies that the asymmetric mode spectrum of the upstream radiated sound field is predominantly determined by the dipole characteristic and orientation of the stator leading edge sources. Further, shielding of rotor counter-rotating modes originating from stator bound sources and rotor bound dipole sources of e.g. trailing edge noise [25] play a role regarding the asymmetry of the inlet mode spectrum.

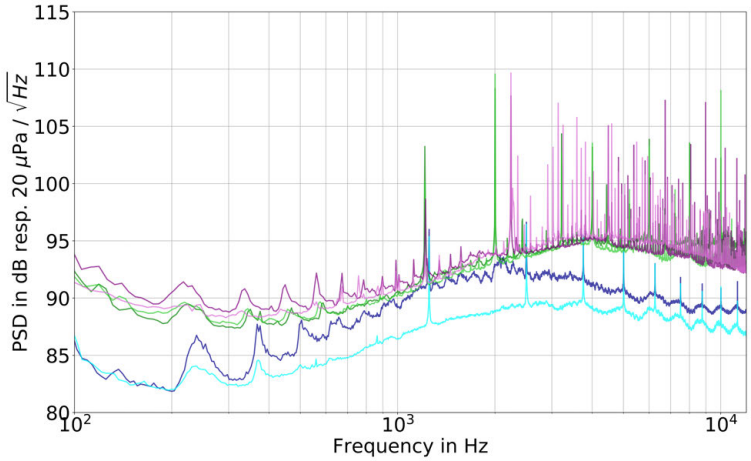

(a) Inlet

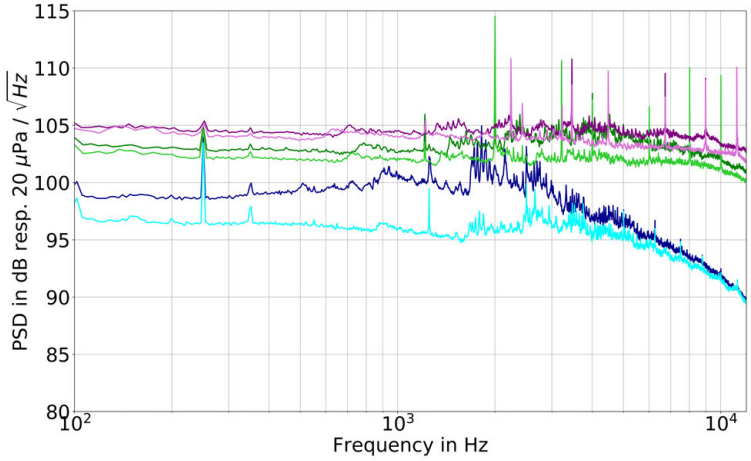

(b) Interstage

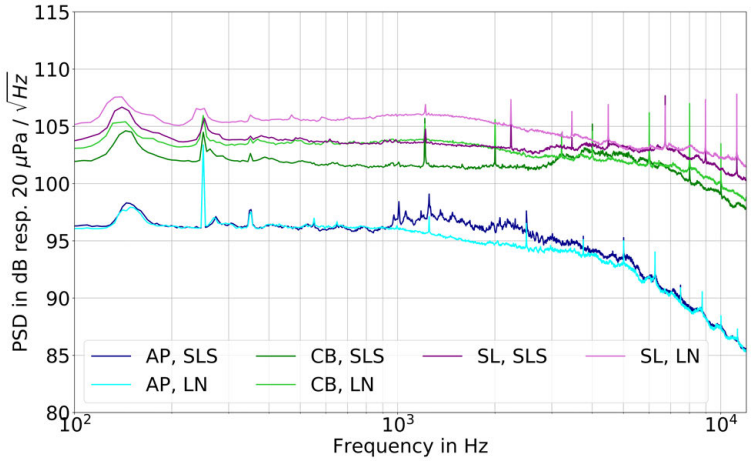

(c) Bypass

Fig. 10 Comparison of the broadband (CyS2) spectra averaged over the ring arrays at inlet, interstage and bypass. The results are shown for the long gap configuration.

The cut-on limits for the sections at the array positions (white lines), the rotor leading edge and stator trailing edge (red lines) and at the stator leading edge in the interstage (yellow lines) give further hints regarding the identification of the dominant sound generation mechanisms. At the bypass section the generated broadband mode spectrum coincides well with the cut-on mode range at the stator trailing edge as was the case for the tonal mode spectrum. This proves that there are no significant noise sources situated downstream of the stator, which could be due to flow separation at the duct widening or reflections and scattering at the outlet nozzle. Further, there is no impact of azimuthal flow inhomogeneities that e.g. may have resulted from rotor wake irregularities remaining also downstream of the stator. The working line comparison reveals the noise reduction to be effective for the lower azimuthal mode orders ($|m| \leq 20$) with a particular effect on the rotor counter-rotating modes.

The sound field radiated upstream towards the inlet exhibits interesting features. It appears that the mode spectrum at LN working line depends on the cut-on mode range at the rotor leading edge (red lines) as well as on the stator leading edge in the interstage (yellow lines). In contrast to the SLS working line it is observed that the modes close to the cut-off limit at the rotor are not excited dominantly at LN working line, which suggests that the main sound generation mechanism is the interaction of the wake turbulence with the stator leading edges. On the other hand, rotor self-noise is the main contributor to the upstream sound field at SLS working line, because the detected mode spectrum matches very well with the cut-on mode range at the rotor. For the upstream radiated sound field the working line comparison shows that the noise reduction is achieved by lower amplitudes of the rotor co-rotating modes.

4. Detailed analysis of the broadband sound generation at high rotor speed

Figure 12 shows the comparison of the resulting tonal and broadband mode spectra at high rotor speeds, exemplarily for the short gap configuration at LN working line and *sideline* condition. Additional results for high speed operating conditions are given in the appendix. The development of shocks at the rotor leading edge due to supersonic flow conditions leads to the occurrence of *buzz-saw* noise at the inlet [17]. The signature of buzz-saw noise follows the relation $m = -EO$, which is seen in both components, tonal and broadband. Related to the increased flow velocity at this operation point the cut-on ranges at the rotor leading edges and at the sensor array in the inlet are inverted, i.e. more modes are cut-on in the vicinity of the rotor. Below engine order 20 this inversion leads to lower mode amplitudes compared to higher engine orders, because the acoustic modes that are excited by the rotating shock pattern decay in the inlet array section. Rotor-stator interaction modes are detected for both, tonal and broadband, components, but they have relatively small amplitudes on account of increased rotor shielding due to the presence of shocks [30]. The broadband mode spectrum differs drastically from the low speed case and it features rotor bound sources, whose contribution is identified by the ray-like structures, which are symmetrically distributed w.r.t. the azimuthal mode order and have a slope of $\pm EO$ indicating the Doppler shift. Besides the *buzz-saw* noise components the tonal mode spectrum does not exhibit contribution of rotor bound sources within the dynamic range of the analysis. This observation shows that apart from the shock-related noise rotor self-noise is generated through interaction of the inflow turbulence with the rotor resulting in broadband sound radiation.

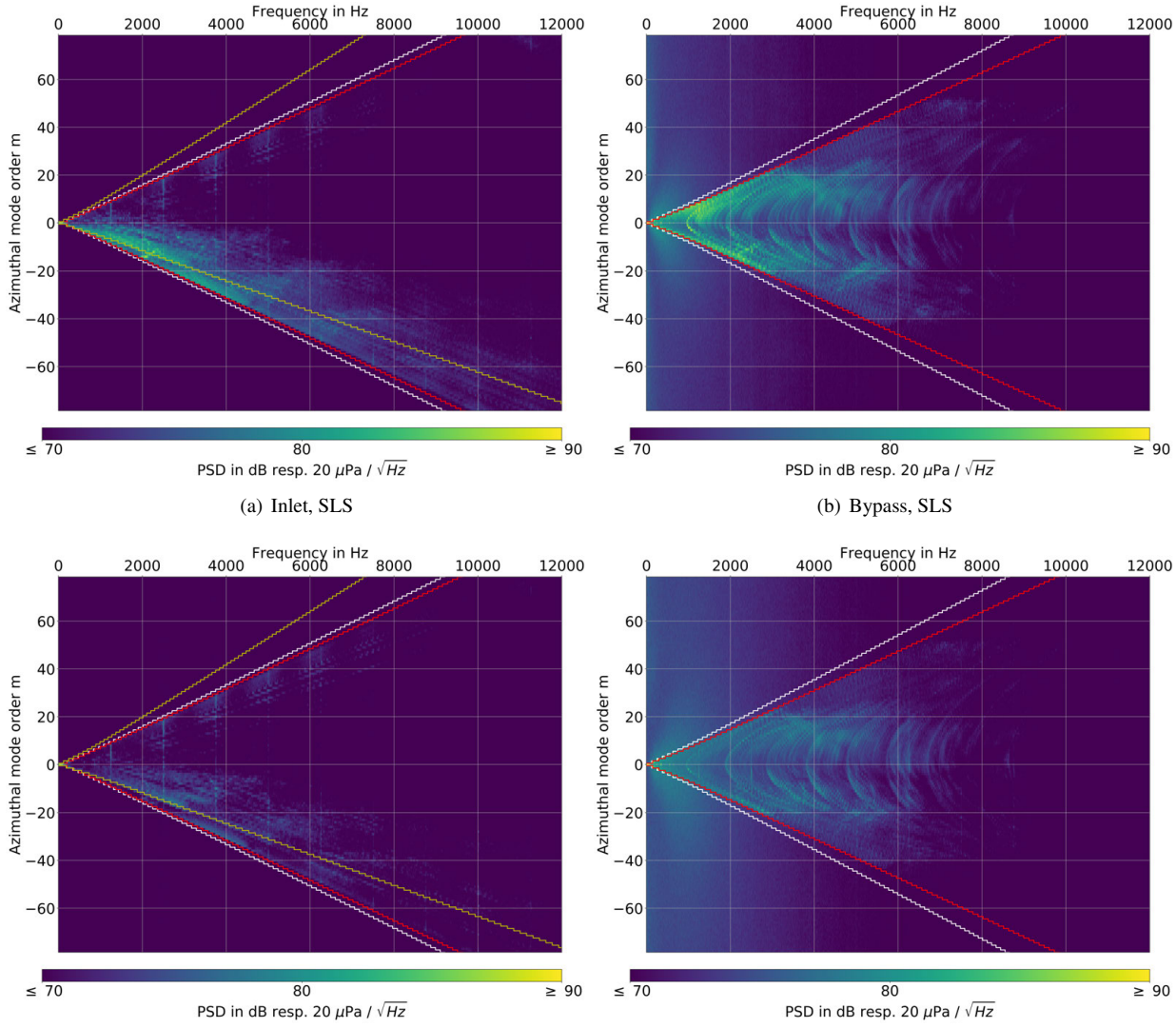

(a) Inlet, SLS

(b) Bypass, SLS

(c) Inlet, LN

(d) Bypass, LN

Fig. 11 Working line comparison of the broadband (CyS2) azimuthal mode spectra for the ring arrays at bypass and inlet. The results are shown for the long gap configuration, SLS and LN working lines at *approach*. The red lines indicate the mode cut-on range at the rotor front face on the left-hand side and at the stator trailing edge on the right-hand side. The white lines show the cut-on range at the respective array positions at the inlet and bypass. The mode cut-on range in the interstage section close to the stator leading edge is given by the yellow lines.

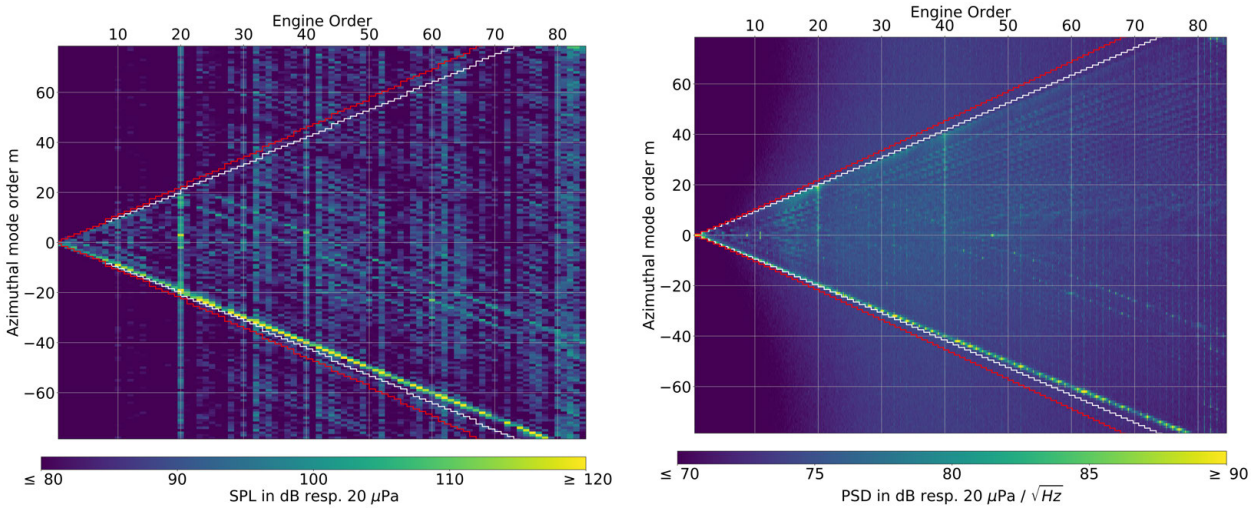

(a) Tonal (CyS1)

(b) Broadband (CyS2)

Fig. 12 Comparison of the tonal (CyS1) and broadband (CyS2) azimuthal mode spectra for the ring array at the inlet section. The results are shown for the short gap configuration, LN working line at *sideline*. The red lines indicate the mode cut-on range at the rotor front face. The white lines show the cut-on range at the array position in the inlet.

VI. Assessment of sound transmission effects through the ACAT1 fan stage

In the following part of the study the sound transmission through the ACAT1 fan stage is investigated with focus on the stator and the downstream radiated sound field. Evidence of mode scattering at the stator vane row is given by evaluation of inter-mode coherences and the corresponding coherent output mode spectrum.

The Compressed Sensing-based mode analysis has the advantage of determining the complete cross-spectral matrix of mode amplitudes, which enables the evaluation of inter-mode coherences. Coherence between pairs of modes is the result of a source or transmission mechanism that affects the respective modes in a similar way. A common assumption for the analysis of broadband sound fields radiated by ducted turbomachinery is that the mode constituents are incoherent. The inter-mode coherence is calculated for each pair of modes at each frequency. The results of the inter-mode coherence[‡] between all combinations of analysed mode orders at 4 kHz shown in Fig. 13 reveal the occurrence of very distinct mode pairs yielding considerable mode coherence in the bypass. Results are shown exemplarily for *cutback* conditions, but same observations are made for *approach* and *sideline* conditions (not shown in this study). The coherent mode pairs differ by the number of stator vanes regarding the azimuthal mode order. This indicates that they are related through mode scattering at the stator vane row. In contrast, mode pairs with slightly increased inter-mode coherence are identified for various values of Δm through the interstage mode analysis, which is caused by the reduced dynamic range of the interstage array compared to the bypass array. Therefore, no conclusive evidence of significant mode coherences is found in the interstage mode analysis. Further, the inlet mode analysis has shown that the modes of different azimuthal mode order are incoherent for the upstream radiated sound field. It is important to note that the presented analysis cannot assess the coherence between radial modes with the same azimuthal mode order and different radial mode order as well as scattered modes at different frequencies that are linked through frequency scattering at the rotor.

The comparison of the working lines SLS and LN reveals that the determined mode coherences are negligible for the LN working line (see Fig. 14), regardless of the operating point. This suggests that mode scattering at the stator depends on the flow conditions in the vicinity of the stator vanes.

For a more comprehensive evaluation of the inter-mode coherences the maximum occurring values are taken for the respective mode orders at each frequency and plotted. Inter-mode coherences occur over a large frequency range starting at about 3 kHz as shown in Fig. 15. Interestingly, the largest coherences are found between 3 and 6 kHz, which is in astonishingly good agreement with the transition range between the sub-resonant and the super-resonant regime described by Kaji and Okazaki [31]. For sub-resonant conditions the wavelength of the mode impinging on the stator row is large compared to the stator pitch and the incident mode is transmitted without the occurrence of mode

[‡]The coherence for $\Delta m = 0$ has the value 1.0 and is omitted for the sake of clarity.

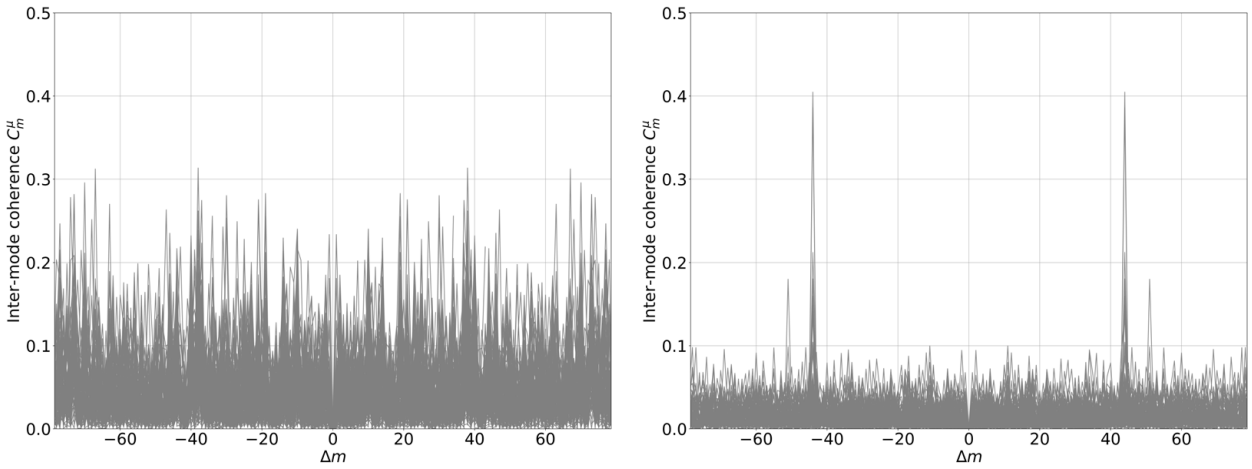

(a) Interstage (b) Bypass

Fig. 13 Comparison of the inter-mode coherences of each azimuthal mode order for the ring arrays at interstage and bypass section at 4 kHz. The results are shown for the long gap configuration, SLS working line at *cutback* and given with respect to $\Delta m = m - \mu$.

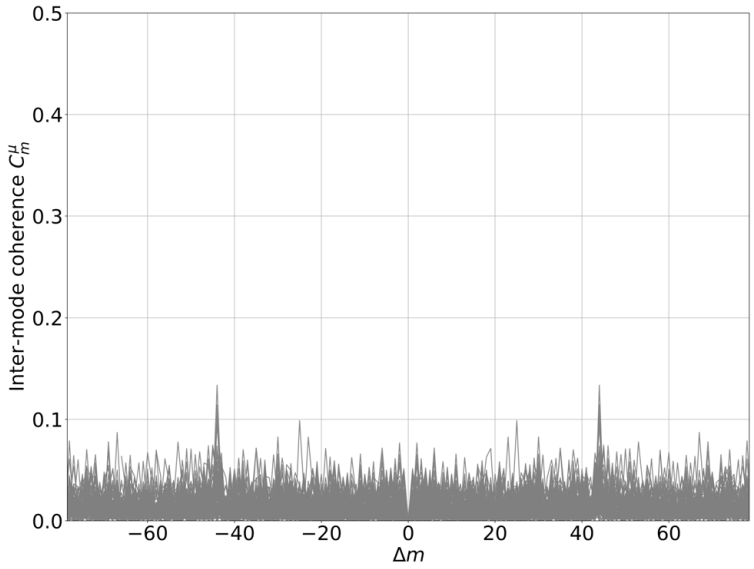

Fig. 14 Inter-mode coherences of each azimuthal mode order in the bypass at 4 kHz. The results are shown for the long gap configuration, LN working line at *cutback* and given with respect to $\Delta m = m - \mu$.

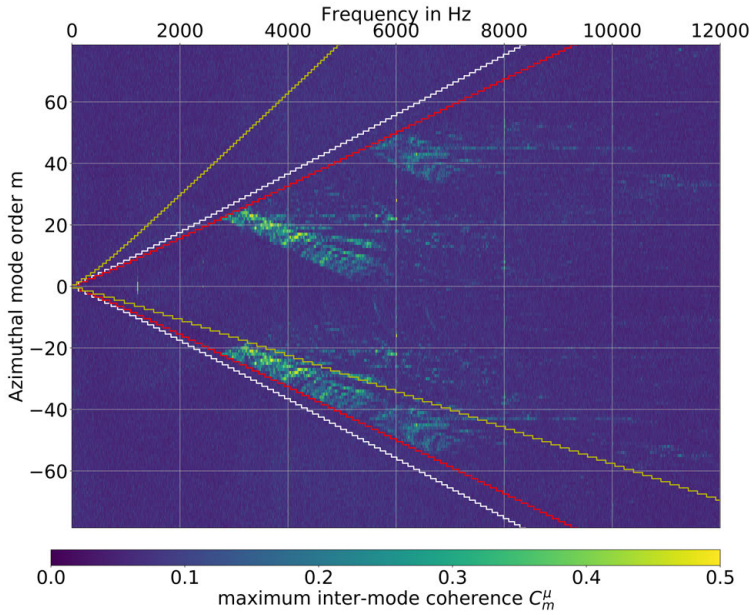

Fig. 15 Maximum inter-mode coherences of each azimuthal mode order in the bypass. The results are shown for the long gap configuration, SLS working line at *cutback*.The red lines indicate the mode cut-on range at the stator trailing edge. The white lines show the cut-on range at the array position at the bypass. The mode cut-on range in the interstage section close to the stator leading edge is given by the yellow lines.

scattering. At super-resonant conditions the wavelength of the impinging mode is smaller than the stator pitch and mode scattering occurs for the transmitted and reflected modes. The transition range can be given in terms of a cascade-related Helmholtz number $\frac{kR}{V}$ with the free-field wavenumber k, the outer radius of the stator vane row R and the number of vanes V. For the sub-resonant regime it holds that $\frac{kR}{V} < 0.5$ and for the super-resonant regime $\frac{kR}{V} > 1$. For the ACAT1 fan stage, the observed frequency limits of 3 and 6 kHz translate to a cascade-related Helmholtz number of $\frac{kR}{V} \approx 0.53$ and $\frac{kR}{V} \approx 1.05$. Another interesting observation is that the range of rotor co-rotating modes, which are involved in the determined mode scattering, lie exactly between the mode cut-on limits at the stator leading (yellow lines) and trailing edges (red lines). These modes are cut-off at the stator leading edge, but become cut-on in the inter-vane channels and contribute to the radiated sound field. This phenomenon was described by Roger et al. [16] as acoustic tunnel effect. As mentioned by Roger et al. so far no evidence of the acoustic tunnel effect has been reported for fan stages.

From the analysis described above the direction of the mode scattering is not determined. This aspect is discussed on the basis of the coherent output mode spectrum defined in Eq. 7, which is the resulting power spectrum due to mode coherence C_m^μ when the mode order m is regarded as the output variable and the mode order μ is the input variable. In Figure 16 the coherent output spectrum are compared for both possible scattering directions, that is for $\Delta m = \pm 44$. The presented results are the sum of all coherent mode amplitudes with $\Delta m = m - \mu = \pm 44$. In order to indicate the fraction of the total power involved in the mode scattering the auto power spectra are given as integrals over the entire mode range and only over the rotor co- ($m < 0$) and counter-rotating modes ($m \geq 0$), respectively. In the sub-resonant regime below 3 kHz the coherent output spectra are similar for both scattering directions. Also the integrated auto power spectra for $m < 0$ and $m \geq 0$ match. Above 3 kHz the coherent output spectra increase corresponding to the occurrence of larger inter-mode coherences. The resulting coherent output spectrum for $\Delta m = +44$, i.e. mode scattering from rotor co-rotating modes to counter-rotating modes, is approximately 1-3 dB above the result for the opposite scattering direction. A similar level difference is seen for the auto power spectra, which may indicate that energy is shifted from the rotor co-rotating to the counter-rotating modes due to mode scattering. In summary, the given analysis suggests that the acoustic tunnel effect plays a role in the broadband sound radiation of the ACAT1 fan stage and that it triggers mode scattering towards rotor counter-rotating modes, particularly at the SLS working line. A more detailed analysis of the relevance of the acoustic tunnel effect is not possible using only the mode detection ring arrays, but it requires unsteady surface pressure measurements in the inter-vane channels. Possibly, numerical simulations of the ACAT1 fan stage can provide comparable data and generate more insight into this phenomenon. The contribution of this effect to the

downstream radiated sound field signifies the importance of accounting for the cut-off/cut-on transition of inter-vane channel modes in analytical prediction tools.

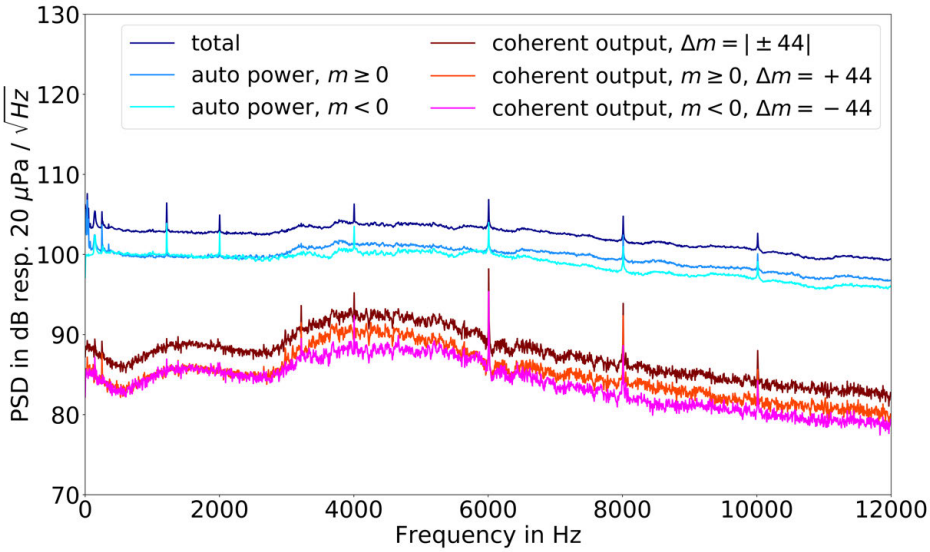

Fig. 16 Coherent output spectrum for mode pairs with $\Delta m = \pm 44$ in comparison to the average auto power spectrum of the ring array in the bypass. The results are shown for the long gap configuration, SLS working line at *cutback*. Spectra are integrated over the range of positive resp. negative mode orders as well as over the entire, analysed mode range.

VII. Conclusion

Azimuthal mode analyses are performed that provide improved accuracy and resolution compared to prior studies because of the optimised geometries of the applied ring arrays, the separation of tonal and broadband sound field components and the application of Compressed Sensing. The results allow deeper insight into the sound generation and transmission mechanisms that contribute to the up- and downstream radiated sound fields. It is found that the range of dominant modes at the measurement sections in the inlet and bypass is determined by the cut-on mode range at the sources. In return, this enables the identification of the contribution of rotor bound and stator bound sources. For instance, the noise reduction of the LN working line in comparison to the SLS working line at *approach* conditions is explained in this way, that rotor self-noise is reduced as a result of improved flow conditions around the rotor blades, so that flow separation at the rotor leading edge is diminished.

The evaluation of interstage mode spectra reveals the occurrence of rotor-coherent modes, whose mode order is equivalent to the respective engine order. By comparison with hotwire data it is shown that these modes originate from rotor wake irregularities and the resulting rotating pressure pattern that scatters into discrete engine order components through the Doppler shift. The newly designed, sparse interstage ring array allows a clear resolution of the azimuthal mode spectrum between rotor and stator and therefore provides the possibility to detect dissimilar rotor wake structures acoustically and without affecting the flow field upstream of the stator or generating additional noise sources. The rotor wake irregularities impede the comparison to results from noise prediction tools, which consider an ideal fan. However, the presence of additional sound field components due to dissimilar rotor wakes makes the ACAT1 dataset more representative for practical applications.

The comparison of the mode spectra at the inlet and interstage facilitates the assessment of the rotor-shielding effect. Modes that spin in opposite direction of the rotor rotation are blocked and do not contribute to the sound field radiated towards the inlet. This effect is observed for both, tonal and broadband, components for modes generated at the stator leading edge through interaction with the rotor wakes. However, for the interstage broadband sound field an asymmetric mode distribution is identified, where rotor co-rotating modes are predominantly excited. The rotor counter-rotating modes have lower amplitudes and hence, the rotor-shielding effect is less significant for the broadband

sound transmission through the rotor. At high rotor speeds, increased rotor self-noise is detected at the inlet, which for the tonal components indicates the presence of shocks at the rotor leading edges leading to *buzz-saw* noise and for the broadband components is embodied in symmetrically distributed, ray-like structures indicating rotor bound sources.

By evaluation of the inter-mode coherences at the bypass section it is observed that mode pairs with $\Delta m = |\pm V| = |\pm 44|$ are partially correlated, which reveals the occurrence of mode scattering at the stator vanes. The results show that modes in particular mode and frequency ranges are scattered at the stator. An astonishingly good approximation for the occurrence of mode scattering is found as the transition range between sub-resonant and super-resonant conditions, given as $0.5 < \frac{kR}{V} < 1.0$ in terms of a cascade-related Helmholtz number. Additionally, a dependence of mode scattering on the flow conditions is identified through comparison of the two working lines, where mode scattering is only found for the SLS working line and mode coherences diminish at the LN working line. From the inter-mode coherences evidence of the acoustic tunnel effect is derived by inspection of the coherent output spectrum. It is found that rotor co-rotating modes, which are excited and cut-off at the stator leading edge, become cut-on in the inter-vane channels and contribute to the downstream radiated sound field significantly through mode scattering into rotor counter-rotating modes.

The reported results show the capabilities of advanced signal processing and the Compressed Sensing-based mode analysis in order to provide high resolution data for the assessment of the sound generation through turbomachinery stages and for the validation of numerical codes in the challenging situation of the presence of rotor wake irregularities. The sound generation and transmission effects observed in the azimuthal mode analyses give suggestions for the advancement of analytical models in order to achieve reliable predictions of realistic configurations like the ACAT1 fan stage.

A. Appendix

A. Tonal (CyS1) mode spectra at the inlet

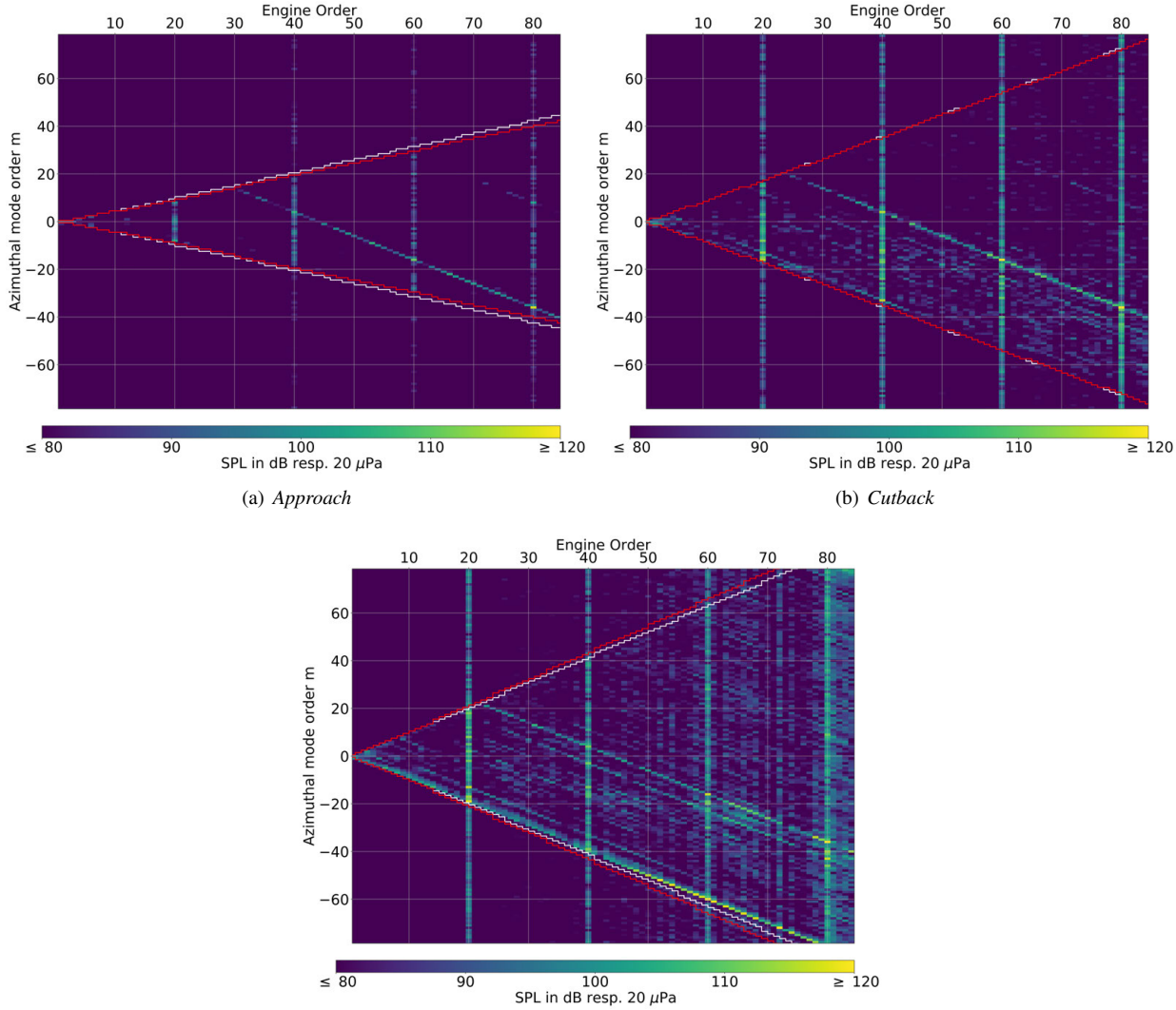

(a) *Approach*

(b) *Cutback*

(c) *Sideline*

Fig. 17 Operating point comparison of the tonal (CyS1) azimuthal mode spectra for the ring arrays at the inlet. The results are shown for the short gap configuration and SLS working line. The red lines indicate the mode cut-on range at the rotor front face. The white lines show the cut-on range at the inlet array position.

B. Tonal (CyS1) mode spectra at the bypass

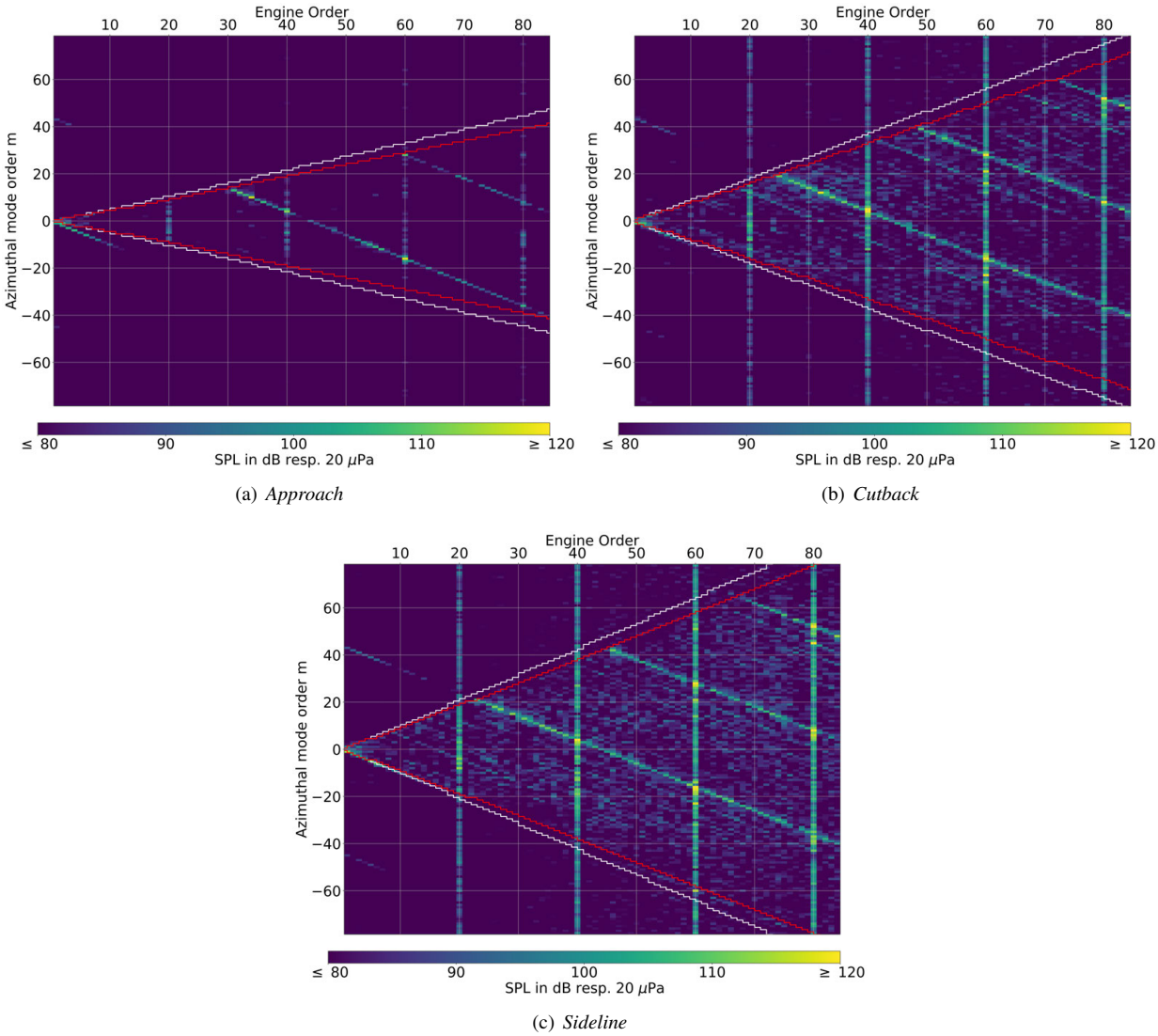

(a) *Approach*

(b) *Cutback*

(c) *Sideline*

Fig. 18 Operating point comparison of the tonal (CyS1) azimuthal mode spectra for the ring arrays at the bypass. The results are shown for the short gap configuration and SLS working line. The red lines indicate the mode cut-on range at the stator trailing edge. The white lines show the cut-on range at the bypass array position.

C. Rotor-alone and interaction modes at tonal (CyS1) components for the long gap configuration

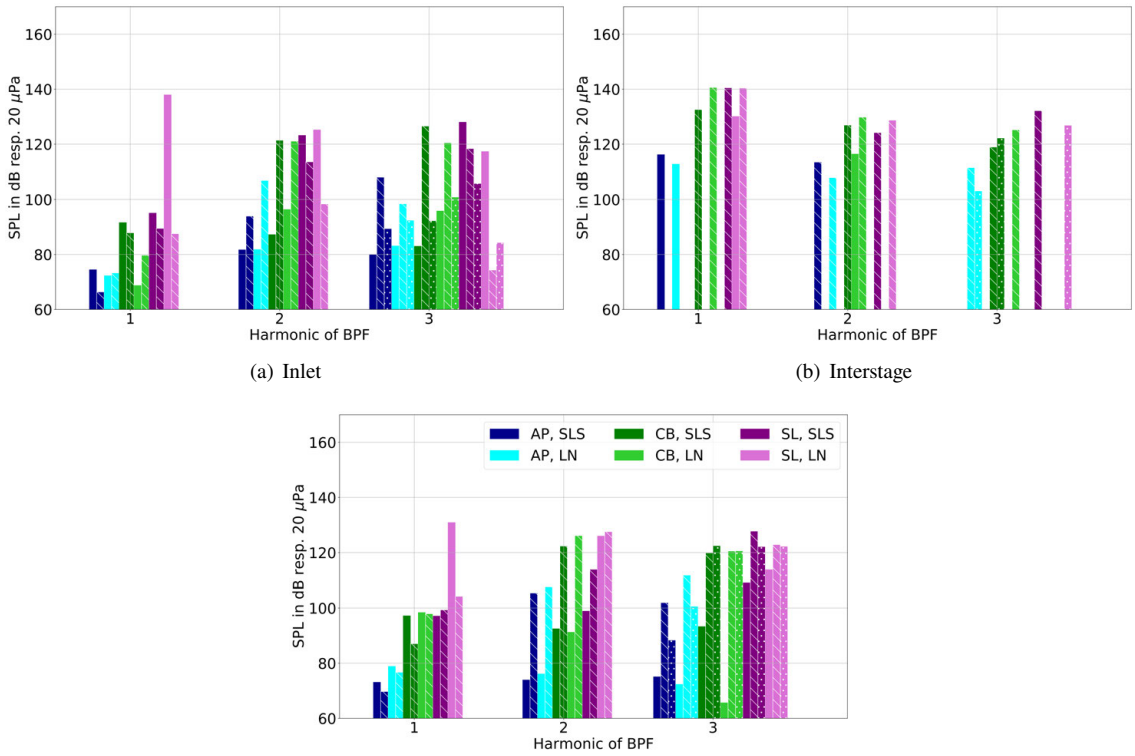

(a) Inlet

(b) Interstage

(c) Bypass

Fig. 19 Comparison of the tonal (CyS1) azimuthal mode spectra for the ring arrays at inlet, interstage and bypass. The results are shown for the long gap configuration. Full bars indicate the rotor-alone mode, hatched bars are the rotor-stator interaction modes.

D. Broadband (CyS2) mode spectra at the inlet

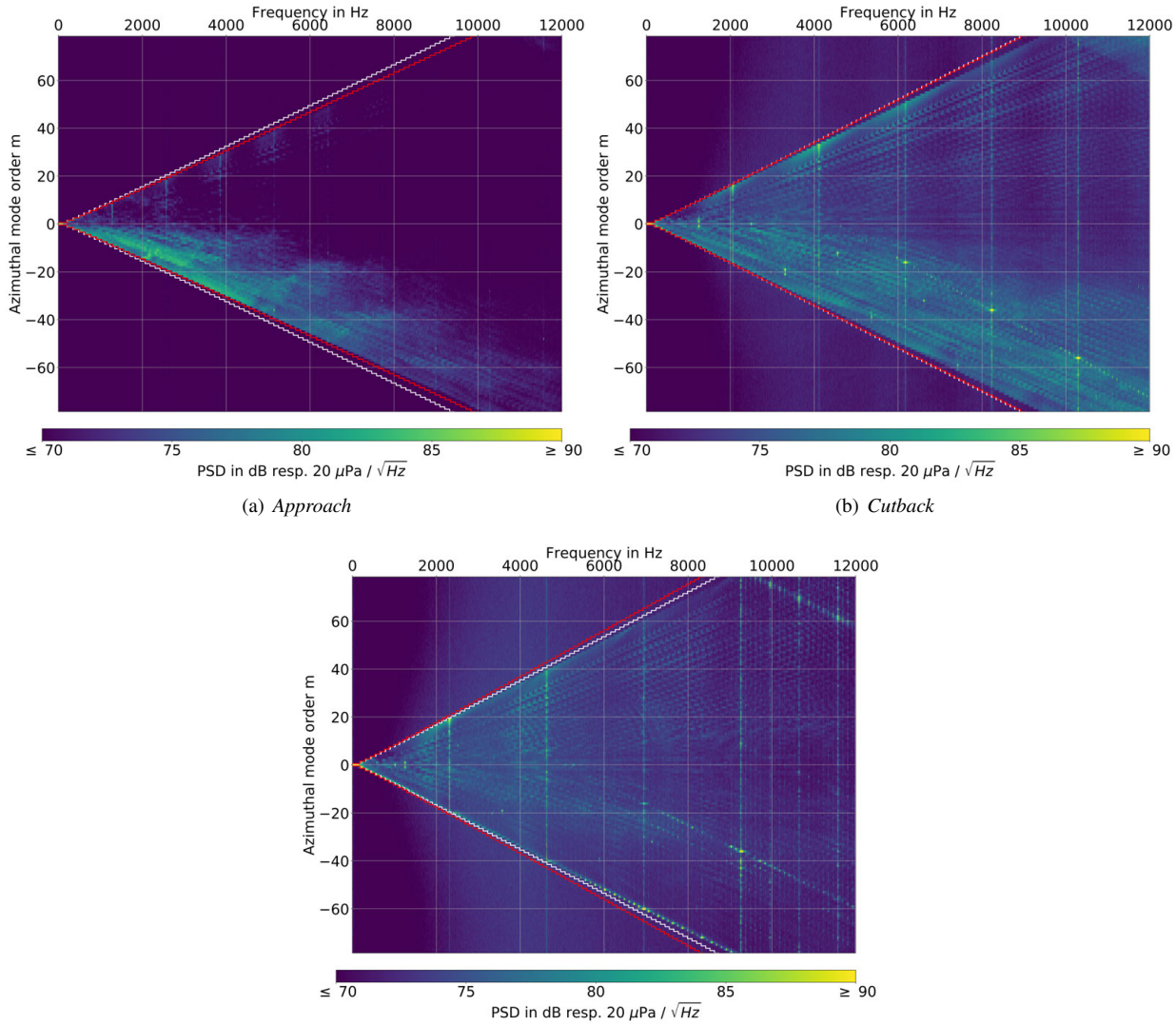

(a) *Approach*

(b) *Cutback*

(c) *Sideline*

Fig. 20 Operating point comparison of the broadband (CyS2) azimuthal mode spectra for the ring arrays at the inlet. The results are shown for the short gap configuration and SLS working line. The red lines indicate the mode cut-on range at the rotor front face. The white lines show the cut-on range at the inlet array position.

E. Broadband (CyS2) mode spectra from the bypass

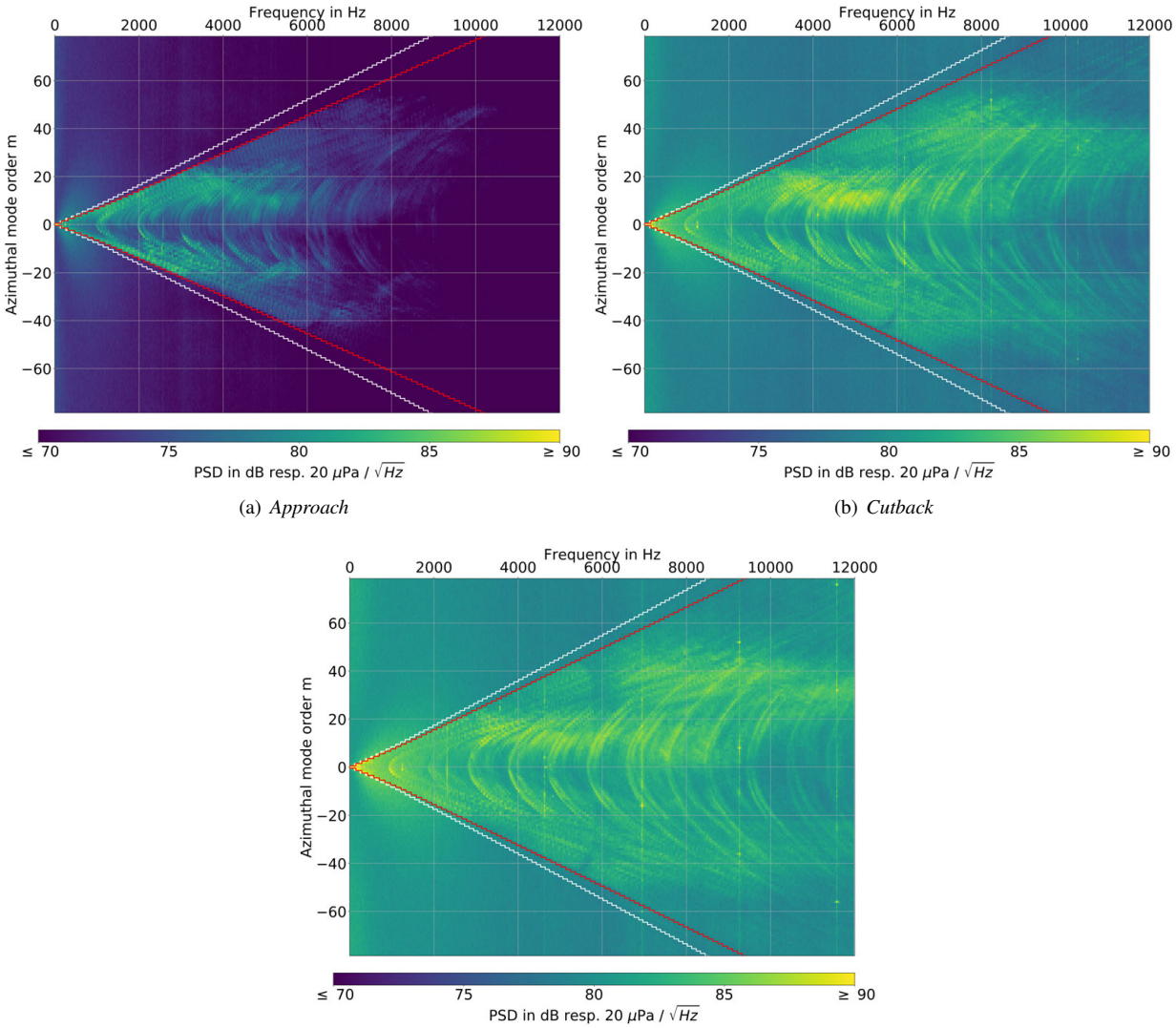

(a) *Approach*

(b) *Cutback*

(c) *Sideline*

Fig. 21 Operating point comparison of the broadband (CyS2) azimuthal mode spectra for the ring arrays at the bypass. The results are shown for the short gap configuration and SLS working line. The red lines indicate the mode cut-on range at the stator trailing edge. The white lines show the cut-on range at the bypass array position.

F. Tonal (CyS1) mode spectra from Interstage for SLS working line

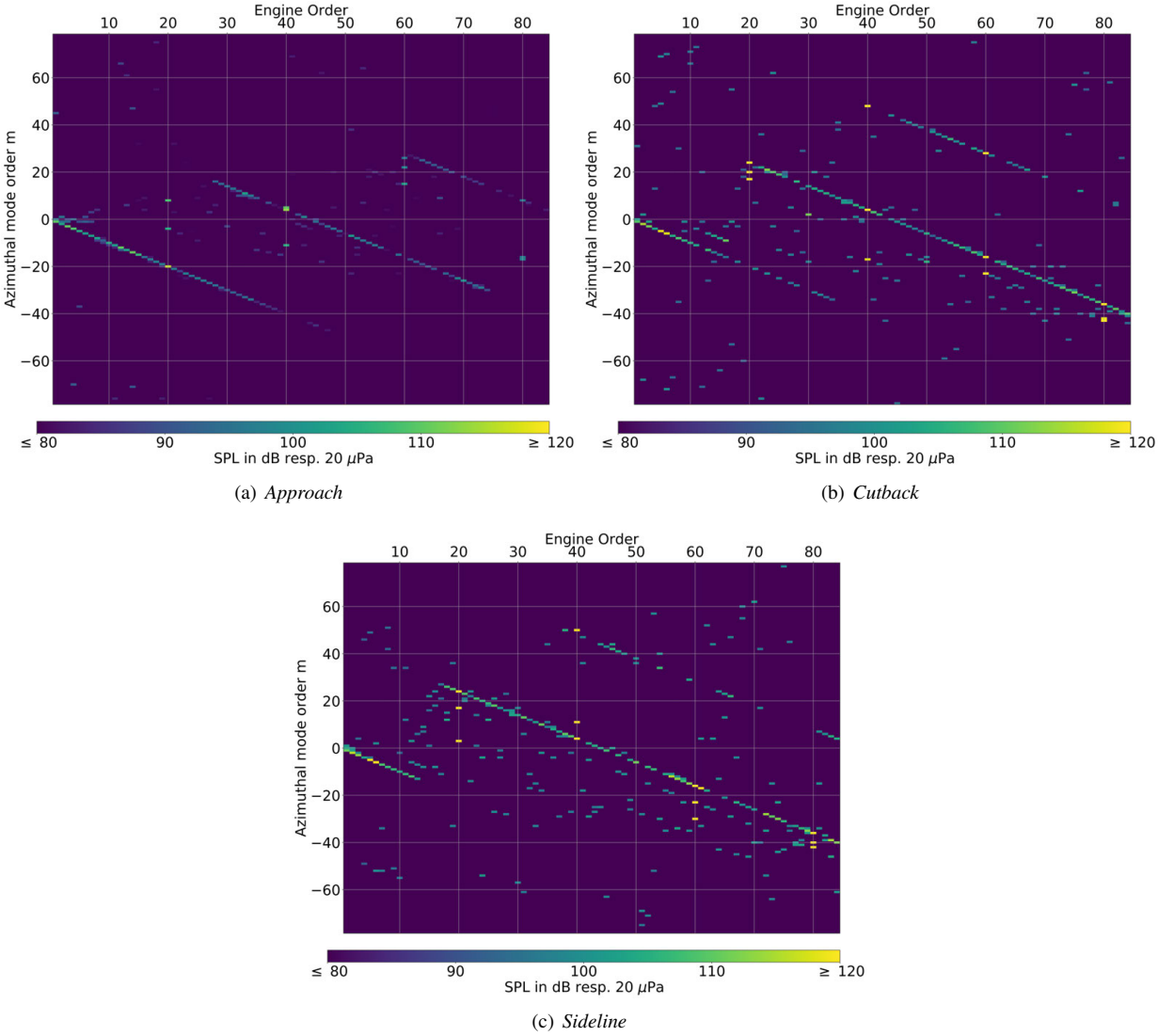

(a) *Approach*

(b) *Cutback*

(c) *Sideline*

Fig. 22 Operating point comparison of the tonal (CyS1) azimuthal mode spectra at the interstage. The results are shown for the long gap configuration, SLS working line at the three operating conditions *approach*, *cutback* and *sideline*.

G. Tonal (CyS1) mode spectra at the interstage for LN working line

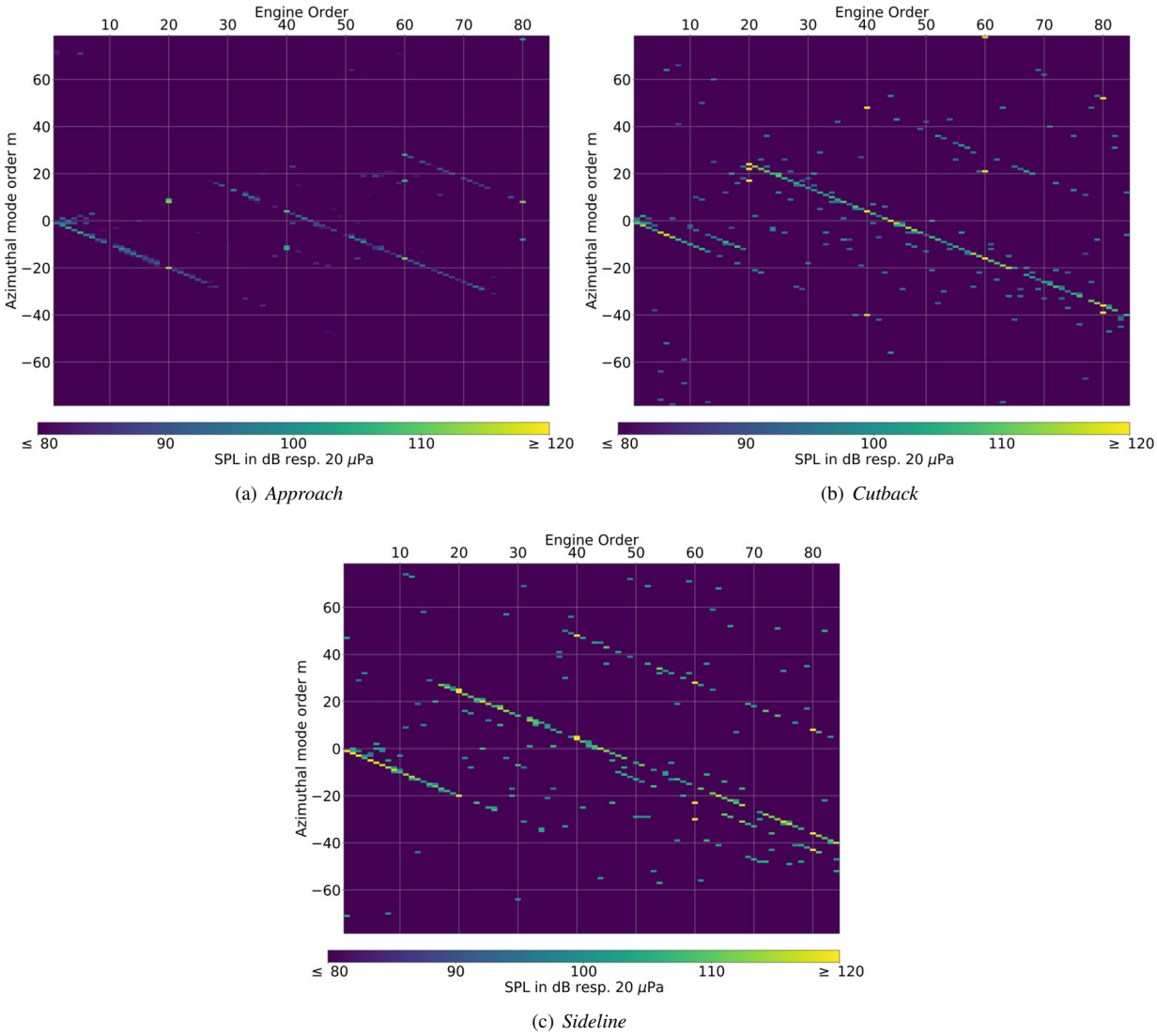

(a) *Approach*

(b) *Cutback*

(c) *Sideline*

Fig. 23 Operating point comparison of the tonal (CyS1) azimuthal mode spectra at the interstage. The results are shown for the long gap configuration, LN working line at the three operating conditions *approach*, *cutback* and *sideline*.

H. Broadband (CyS2) mode spectra at the interstage for SLS working line

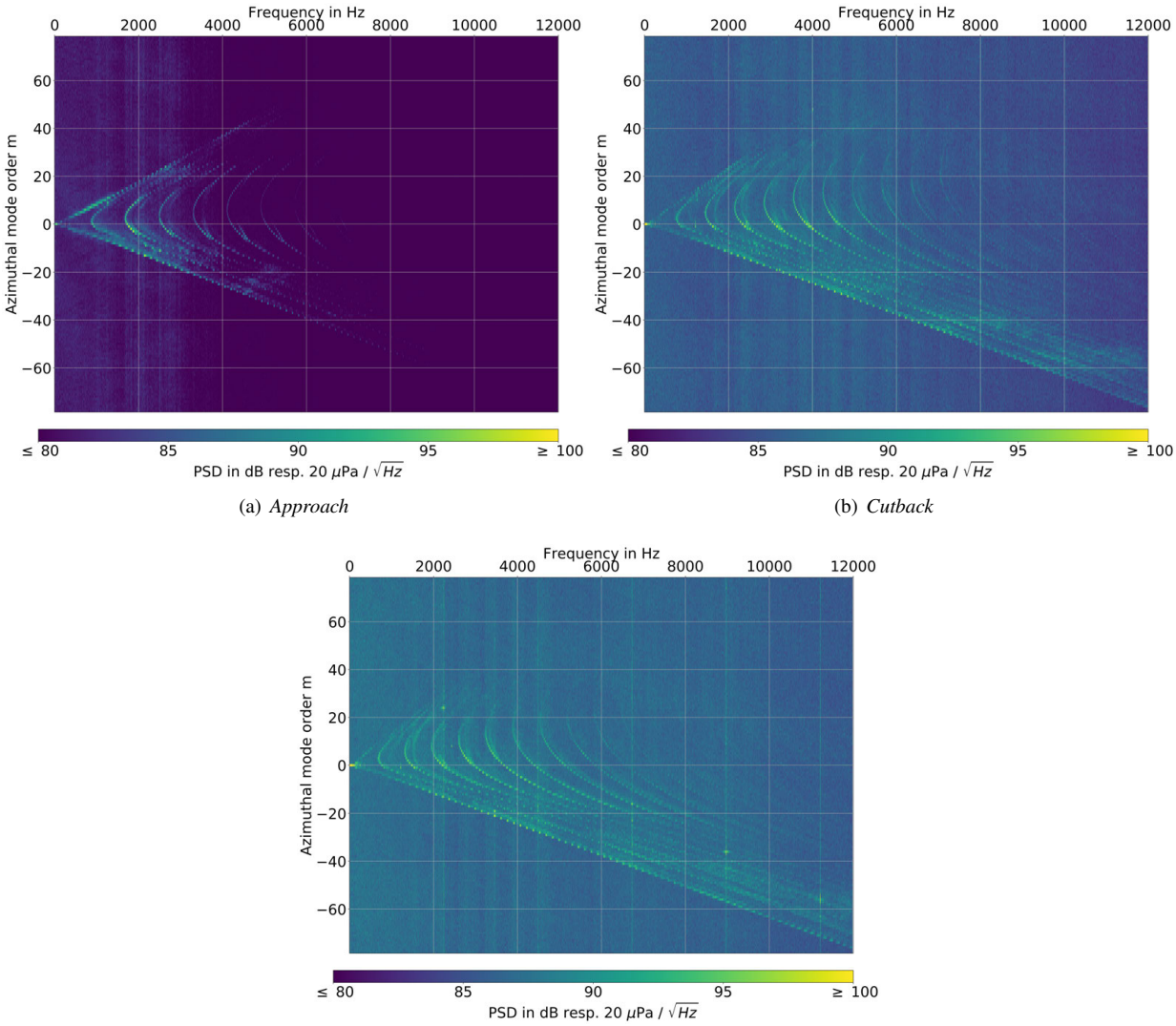

(a) *Approach*

(b) *Cutback*

(c) *Sideline*

Fig. 24 Operating point comparison of the broadband (CyS2) azimuthal mode spectra at the interstage. The results are shown for the long gap configuration, SLS working line at the three operating conditions *approach*, *cutback* and *sideline*.

I. Broadband (CyS2) mode spectra at the interstage for LN working line

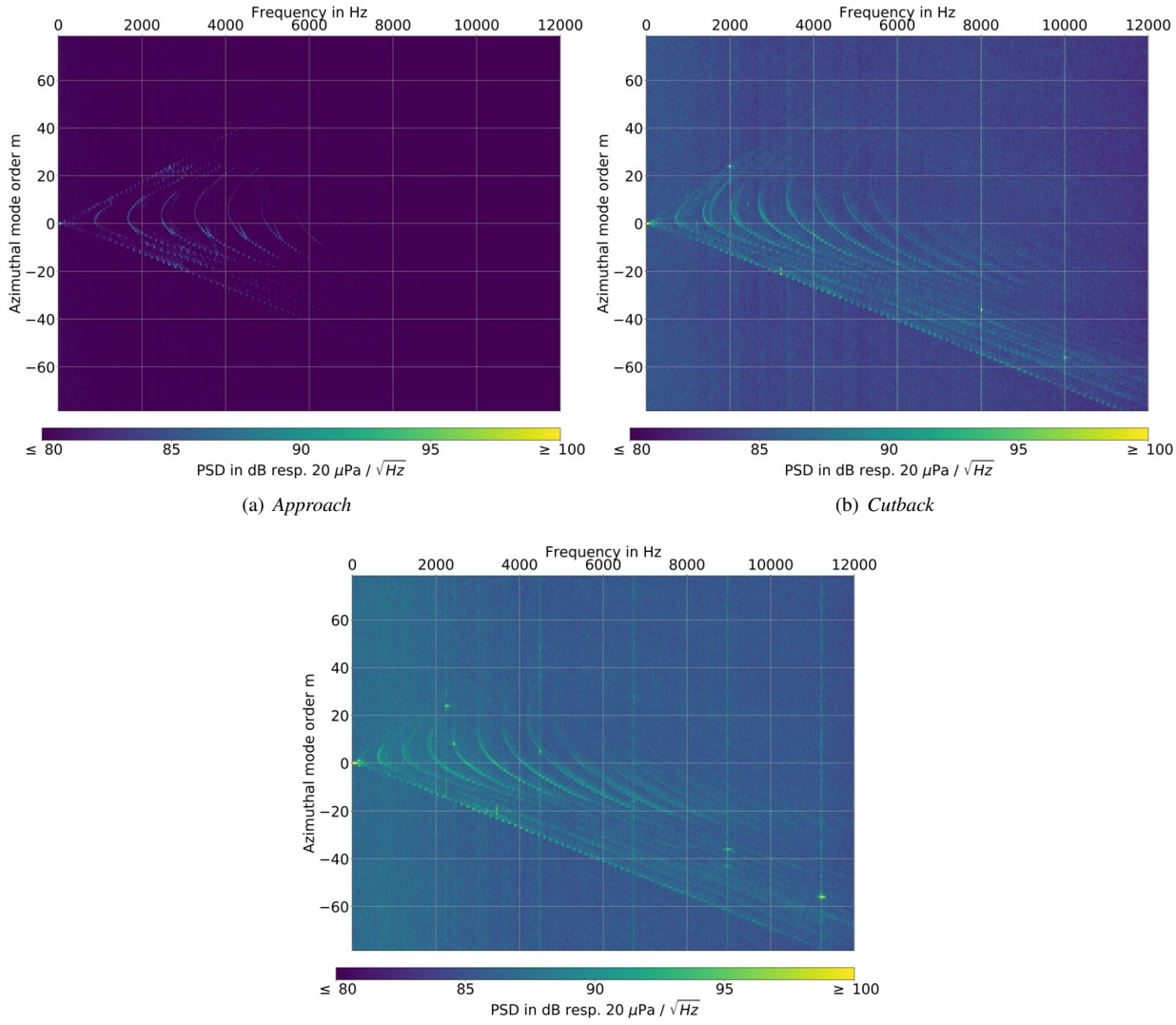

(a) *Approach*

(b) *Cutback*

(c) *Sideline*

Fig. 25 Operating point comparison of the broadband (CyS2) azimuthal mode spectra at the interstage. The results are shown for the long gap configuration, LN working line at the three operating conditions *approach*, *cutback* and *sideline*.

Acknowledgments

The presented investigation was conducted within the project TurboNoiseBB with funding from Horizon 2020 research and innovation program of the European Union under grant agreement No. 690714.
The authors are very grateful to all the participants of the test campaign, in particular Wolfram Hage and Benjamin Pardowitz (DLR), Karsten Liesner and the rest of the staff of AneCom AeroTest, Wolfgang Weith and Nick Crowder (Rolls-Royce), Azucena Pintado and Thomas Nodé-Langlois (Airbus).
The authors acknowledge gratefully the provision of the hotwire data by Robert Meyer and Sebastian Hakansson (DLR).

References

[1] Tyler, J. M., and Sofrin, T. G., "Axial Flow Compressor Noise Studies," *SAE Transactions*, Vol. 70, 1962, pp. 309–332.

[2] Joseph, P., Morfey, C., and Lowis, C., "Multi-mode sound transmission in duts with flow," *Journal of Sound and Vibration*, Vol. 264, 2003, pp. 523–544.

[3] Mugridge, B., "The measurement of spinning acoustic modes generated in an axial flow fan," *Journal of Sound and Vibration*, Vol. 10, No. 2, 1969, pp. 227–246.

[4] Moore, C., "Measurement of radial and circumferential modes in annular and circular fan ducts," *Journal of Sound and Vibration*, Vol. 62, No. 2, 1979, pp. 235–256.

[5] Bolleter, U., and Crocker, M., "Theory and measurement of modal spectra in hard-walled cylindrical ducts," *Journal of the Acoustical Society of America*, Vol. 51, 1972, pp. 1439–1447.

[6] Kerschen, E., and Johnston, J., "A modal separation measurement technique for broadband noise propagating inside circular ducts," *Journal of Sound and Vibration*, Vol. 76, No. 4, 1981, pp. 499–515.

[7] Heidelberg, L. J., "Fan Noise Source Diagnostic Test - Tone Modal Structure Results," *8th AIAA/CEAS Aeroacoustics Conference*, Breckenridge, Colorado (USA), 2002. AIAA 2002-2428.

[8] Premo, J., and Joppa, P., "Fan Noise Source Diagnostic Test - Wall Measured Circumferential Array Mode Results," *8th AIAA/CEAS Aeroacoustics Conference*, Breckenridge, Colorado (USA), 2002. AIAA 2002-2429.

[9] Sijtsma, P., and Brouwer, H., "Deconvolution of azimuthal mode detection measurements," *Journal of Sound and Vibration*, Vol. 422, 2018, pp. 1–14.

[10] Dougherty, R. P., and Bozak, R., "Two-dimensional Modal Beamforming in Wavenumber Space for Duct Acoustics," *24th AIAA/CEAS Aeroacoustics Conference*, Atlanta, Georgia (USA), 2018. AIAA 2018-2805.

[11] Huang, X., "Compressive Sensing and Reconstruction in Measurements with an Aerospace Application," *AIAA Journal*, Vol. 51, No. 4, 2013. doi:10.2514/1.J052227, technical note.

[12] Behn, M., Kisler, R., and Tapken, U., "Efficient Azimuthal Mode Analysis using Compressed Sensing," *22nd AIAA/CEAS Aeroacoustics Conference*, Lyon, France, 2016. AIAA 2016-3038.

[13] Behn, M., Pardowitz, B., and Tapken, U., "Compressed Sensing based radial mode analysis of the broadband sound field in a low-speed fan test rig," *7th Berlin Beamforming Conference*, Berlin, Germany, 2018. BeBeC-2018-D26.

[14] Bu, H., Yu, W., Kwan, P.-W., and Huang, X., "Wind-Tunnel Investigation on the Compressive-Sensing Technique for Aeroengine Fan Noise Detection," *AIAA Journal*, Vol. 56, No. 9, 2018, pp. 3536–3546.

[15] Hurst, J., Behn, M., Tapken, U., and Enghardt, L., "Detection of the dominant acoustic modes emitted by turbomachinery using compressed sensing," *45th International Congress on Noise Control Engineering INTER-NOISE 2016*, Hamburg, Germany, 2016.

[16] Roger, M., and François, B., "Combined analytical models for sound generation and transmission in cambered axial-flow outlet guide vanes," *European Journal of Mechanics B/Fluids*, Vol. 61, 2017, pp. 218–225.

[17] Guérin, S., Kissner, C., Kajasa, B., Jaron, R., Behn, M., Hakansson, S., Pardowitz, B., Tapken, U., Meyer, R., and Enghardt, L., "Noise prediction of the ACAT1 fan with a RANS-informed analytical method: success and challenge," *Submitted to: 25th AIAA/CEAS Aeroacoustics Conference*, Delft, The Netherlands, 2019.

[18] Rademaker, E., Sijtsma, P., and Tester, B., "Mode detection with an optimised array in a model turbofan engine intake at varying shaft speeds," *7th AIAA/CEAS Aeroacoustics Conference*, Maastricht, The Netherlands, 2001. AIAA 2001-2181.

[19] Meyer, R., Hakansson, S., Hage, W., and Enghardt, L., "Instantaneous Flow Field Measurements in the Interstage Section between a Fan and the Outlet Guiding Vanes at Different Axial Positions," *Submitted to: Proceedings of 12th European Conference on Turbomachinery Fluid dynamics and Thermodynamics*, Lausanne, Switzerland, 2019. ETC2019-330.

[20] Antoni, J., "Cyclostationarity by examples," *Mechanical Systems and Signal Processing*, Vol. 23, 2009, pp. 987–1036.

[21] Behn, M., Pardowitz, B., and Tapken, U., "Separation of tonal and broadband noise components by cyclostationary analysis of the modal sound field in a low-speed fan test rig," *fan2018*, Darmstadt, Germany, 2018. Paper-No. 043.

[22] Welch, P., "The Use of Fast Fourier Transform for the Estimation of Power Spectra: A Method Based on Time Averaging Over Short, Modified Periodograms," *IEEE Transactions on Audio and Electroacoustics*, Vol. 15, No. 2, 1967, pp. 70–73.

[23] Nelson, P., and Elliott, S. (eds.), *Active Control of Sound*, Academic Press, London, 1999.

[24] Suzuki, T., "L1 generalized inverse beam-forming algorithm resolving coherent/incoherent, distributed and multipole sources," *J. Sound Vib.*, Vol. 330, 2011, pp. 5835–5851.

[25] Lowis, C. R., and Joseph, P. F., "Determining the strength of rotating broadband sources in ducts by inverse methods," *Journal of Sound and Vibration*, Vol. 295, 2006, pp. 614–632.

[26] Heo, Y.-H., Ih, J.-G., and Bodén, H., "In-duct identification of a rotating sound source with high spatial resolution," *Journal of Sound and Vibration*, Vol. 357, 2015, pp. 51–73.

[27] Goldstein, M. E., "Aeroacoustics," Tech. Rep. SP-346, NASA, 1974.

[28] Sijtsma, P., "Using Phased Array Beamforming to Identify Broadband Noise Sources in a Turbofan Engine," *International Journal of Aeroacoustics*, Vol. 9, No. 3, 2010, pp. 357–374.

[29] Kissner, C., Guérin, S., and Behn, M., "Assessment of a 2D Synthetic Turbulence Method for Predicting the ACAT1 Fan's Broadband Noise," *Submitted to: 25th AIAA/CEAS Aeroacoustics Conference*, Delft, The Netherlands, 2019.

[30] Jenkins, G., Joseph, P. F., and Powles, C. J., "Multimode blockage due to rotors and application to turbomachinery broadband noise," *18th AIAA/CEAS Aeroacoustics Conference*, Colorado Springs, Colorado (USA), 2012. AIAA 2007-3439.

[31] Kaji, S., and Okazaki, T., "Propagation of sound waves through a blade row: II. Analysis based on the acceleration potential method," *Journal of Sound and Vibration*, Vol. 11, No. 3, 1970, pp. 355–375.